Energy &
Environmental
Science

REVIEW

View Article Online
View Journal

Cite this: DOI: 10.1039/d0ee02996c

Received 17th September 2020,
Accepted 12th January 2021

DOI: 10.1039/d0ee02996c

rsc.li/ees

Engineering electrodes and metal halide perovskite materials for flexible/stretchable perovskite solar cells and light-emitting diodes

Kyung-Geun Lim, †[a] Tae-Hee Han†[b] and Tae-Woo Lee *[c]

Organic–inorganic hybrid metal halide perovskites have excellent optoelectronic properties and are soft and resilient; therefore, they are appropriate for use in flexible and stretchable electronic devices. Commercialization of these perovskite optoelectronics requires development of flexible and stretchable electrodes that are compatible with perovskite optoelectronic properties. Compared to optoelectronic organic semiconductors, exploitation of the advantages of perovskite optoelectronics requires new perspectives in flexible and stretchable electrodes. Here we describe techniques to control the optical, electrical, and mechanical properties of metal halide perovskites that must be suitable for use in flexible and stretchable applications, and then discuss the most convincing candidates for flexible and stretchable electrode materials such as conducting polymers, low-dimensional carbon materials, and structured metals and their composites.

Broader context

In recent years, flexible and stretchable perovskite optoelectronic devices such as perovskite solar cells (PeSCs) and perovskite light-emitting diodes (PeLEDs) are highly expected to be used in advanced wearable optoelectronic applications due to the versatile advantages of metal halide perovskites (MHPs). However, the optical, electrical, and mechanical properties of electrodes and MHPs in the devices must be engineered for flexible and stretchable device applications. In this work, the various strategies for MHPs (*e.g.*, composition and additive engineering for mechanical durability and chemical stability) and electrode materials (*e.g.*, conducting polymers, low-dimensional carbon materials, or structured metals and their composites) are systematically suggested to satisfy the multiple requirements of flexible and stretchable PeSCs or PeLEDs. The strategies and perspectives in this work would be a comprehensive research guide for flexible and stretchable PeSCs and PeLEDs.

1. Introduction

Flexible and stretchable metal halide perovskites (MHPs) are mechanically soft and have excellent optoelectronic properties, and therefore have potential applications as elements of inexpensive portable, wearable photovoltaics or displays, or of bio-medical applications and surveillance.[1–4] The mechanical properties of perovskite optoelectronic devices that use flexible and stretchable electrodes can be improved to achieve appropriate resilience to bending and stretching stress. Furthermore, perovskites and flexible electrodes are compatible with mass-production methods.

To enable practical wearable applications of MHPs, the active layer that uses perovskite materials should provide better mechanical stability than that of intrinsic perovskite single crystals. The study of structural influences on the mechanical properties of MHPs is important, and further engineering technology for perovskite poly- or nano-crystals must be conducted to achieve the mechanical requirements for flexible or stretchable electronics. Flexible and stretchable electrodes in optoelectronics must also simultaneously meet requirements for properties such as conductivity, transparency, resilience, robustness, and compatibility with current methods of fabrication.

The interface between electrode materials and photoactive perovskite layers must have appropriate qualities. For example, electron–hole pairs in halide perovskites have small exciton binding energy, therefore dissociate easily at room temperature,

---

[a] *Korea Research Institute of Standards and Science (KRISS), 267 Gajeong-ro, Yuseong-gu, Daejeon 34113, Republic of Korea*
[b] *Division of Materials Science and Engineering, Hanyang University, 222 Wangsimni-ro, Seongdong-gu, Seoul, 04763, Republic of Korea*
[c] *Department of Materials Science and Engineering, School of Chemical and Biological Engineering, Research Institute of Advanced Materials, Institute of Engineering Research, Nano Systems Institute (NSI), Seoul National University, 1 Gwanak-ro, Gwanak-gu, Seoul 08826, Republic of Korea. E-mail: twlees@snu.ac.kr, taewlees@gmail.com*

† These authors contributed equally to this work.

and their carrier diffusion length can be much longer than in organic materials.[5] The conventional metal oxide electrodes (*e.g.*, indium-tin-oxide, ITO) in perovskite solar cells (PSCs) or perovskite light-emitting diodes (PeLEDs) release metal atoms, so the luminescence quenching and charge trapping near the electrode is more severe than in organic solar cells (OSCs) or organic light-emitting diodes (OLEDs).[6–8] Therefore, to achieve both flexibility or stretchability and high device efficiency, use of flexible and stretchable non-oxide electrodes is more important in perovskite optoelectronics than in the conventional organic counterparts. Also, the flexible and stretchable electrodes that use various non-oxide conducting materials must be further engineered to improve the optoelectronic and mechanical properties of PSCs and PeLEDs. Commercialization of PSCs that use synthetic non-oxide materials can be made feasible by overcoming the relatively insufficient resilience of PSCs compared to OPVs. Synthetic functionalized electrodes or interface materials can increase the robustness and prolong the lifetime and change period of PSC panels. Therefore, flexible and stretchable electrodes that use synthetic non-oxide materials increase the resilience and the marketability of perovskite optoelectronics.

This paper reviews recent advances in interface and electrode materials for highly-efficient and reliable operation of flexible and stretchable perovskite optoelectronics. These devices consist of a substrate, bottom and top electrodes, charge transfer layers (CTLs), and a perovskite layer (Fig. 1). The new candidate materials for use in the electrodes (*e.g.*, conducting polymers, low-dimensional carbon, and metal composite materials) and CTLs (*e.g.*, organic semiconductors, metal oxides (MOs), and ultra-thin interfacial materials) can be categorized according to their conductivity, transparency, resilience, robustness, and ease of fabrication.

Here we review multiple approaches to fabricate flexible and stretchable electrodes for perovskite optoelectronics, especially PSCs and PeLEDs.

In Section 2, we review the mechanical properties of MHPs and studies on how their constituents affect the mechanical properties of the perovskite. We also consider engineering strategies such as organic additives, polycrystal engineering, and nanocrystal–polymer composites to increase the mechanical flexibility and stretchability of halide perovskite layers.

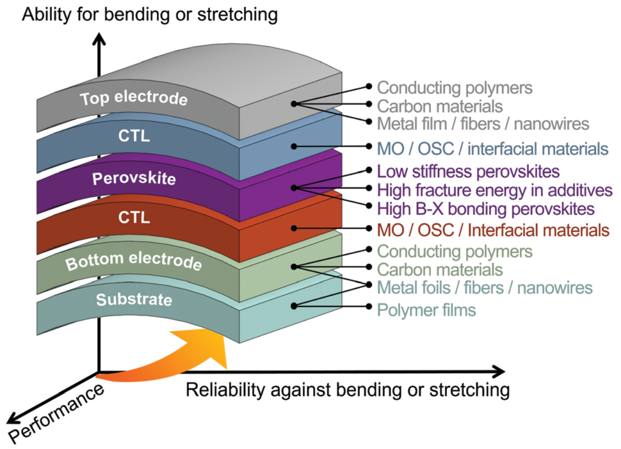

Fig. 1 Functions and strategies of flexible and stretchable electrodes for perovskite optoelectronics.

In Section 3, we review advanced and novel approaches that use conducting polymers, low-dimensional carbons, structured metals and their composites to obtain flexible and stretchable perovskite optoelectronics. We review transparent electrodes that use conducting polymers, and then explain the material properties and the strategies to apply conducting polymers to flexible and stretchable perovskite optoelectronics. We also review conductive low-dimensional carbon materials used in perovskite optoelectronics. We also review the use of the structured metals of metal foils or fibers as conductive substrates, and the use of metal composite materials (*e.g.* nanoscale materials or thin-film metals or metal oxides (MOs)) as transparent electrodes.

In Section 4, we summarize the trends, and provide perspectives for further advancement of this field.

2. Control of the mechanical properties of MHPs

MHPs may have applications in flexible and stretchable devices. In addition to excellent optoelectronic properties, MHPs are softer than inorganic photoactive materials, due to their ductile properties depending on the A-site cation and inorganic framework (B–X bonding). Therefore, many researchers have studied the mechanical properties of MHPs to assess their feasibility for use in next-generation optoelectronic applications. MHPs also emit light in a narrow band, and this property widens their possible applications to include wearable high-color-purity displays and narrow-band biomedical devices.[9–12]

MHPs (ABX_3, where A and B are cations and X is a halide) have good ductile properties, which are mostly attributed to a low shear modulus with a high degree of anisotropy, and to low mechanical hardness of the crystals.[9,12] The selection of the organic components in the MHP structure allows tuning of the mechanical and optoelectronic properties. The mechanical properties of MHPs are more affected by the inorganic framework comprising halide and metal ions than by the A-site cations. The bonding strength and the flexibility of the metal–halide (B–X) bond have an important influence on the B–X framework's mechanical stiffness, so the electronegativity of the halide is also an important factor.[13,14] Compared to single crystal perovskites, the polycrystalline perovskites that are usually used in perovskite optoelectronic devices are much more nanoductile and fracture-resistant due to substantial amorphization of polycrystals.[15] In this section, the influencing factors on the mechanical properties of MHPs are thoroughly reviewed, and the approaches to form intrinsically stretchable photoactive layers based on perovskite nanocrystals are also introduced.

2.1. A-site cation

Many researchers believe that an organic cation at the A site has a strong influence on the soft characteristics of MHPs, but an organic–inorganic hybrid perovskite ($CH_3NH_3PbBr_3$) and an inorganic perovskite (CsPbBr) do not differ much in their mechanical properties under elastic or plastic deformation.[12] Furthermore, the organic cation in MHPs may just provide a balancing charge and fill the cavity between Pb–X frameworks; if so, it does not have a large influence on the mechanical properties.[16]

Some reports suggested that the A-site cation in MHPs merely determines the strength and configurations of hydrogen bonding with the B-site metal components. *Ab initio* molecular dynamics (AIMD) calculations[13] on the influence of the organic cations in a lead bromide perovskite ($APbBr_3$) with the methyl ammonium ion ($CH_3NH_3^+$, MA^+) and formamidinium ion ($C_3N_2H_5^+$, FA^+) suggested that the closest N···Br interatomic distance was correlated with the strength of hydrogen bonding between the organic cation and bromine in the lead bromide perovskites. The radial distribution calculation suggested that the closest N···Br distance was shorter (3.38 Å) in $MAPbBr_3$ than in $FAPbBr_3$ (3.48 Å) while the closest C···Br distance was longer in $MAPbBr_3$ (3.73 Å) than in $FAPbBr_3$ (3.63 Å) (Fig. 2a and b); the difference may be directly translated to larger hydrogen bonding strength in $MAPbBr_3$ than in $FAPbBr_3$. Consequently, the lower stiffness of $FAPbBr_3$ ($E \sim 11.5$ GPa) than that of $MAPbBr_3$ (17.7 GPa) may be a result of the lower hydrogen bonding strength between FA^+ and the inorganic framework than between MA^+ and the inorganic framework (Fig. 2c).[13]

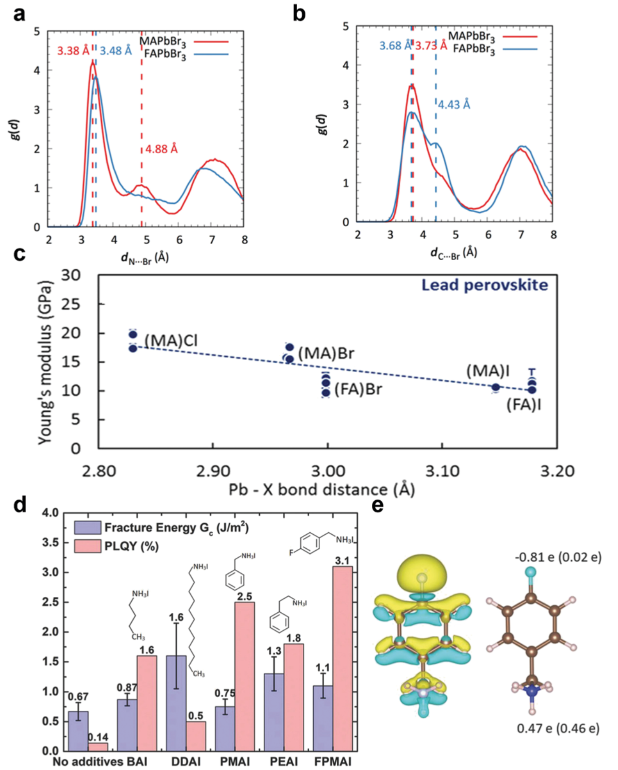

Fig. 2 Radial distribution function of (a) N···Br, and (b) C···Br in $MAPbBr_3$ and $FAPbBr_3$,[13] (c) Young's modulus of MA and FA based halide perovskites with various halides (MACl, MABr, FABr, MAI, and FAI),[13] (Reproduced from ref. 13 with permission from John Wiley and Sons.) (d) fracture energy and photoluminescence quantum yield for MHPs without or with butylammonium iodode (BAI), dodecylammonium iodide (DDAI), benzylammonium iodide (PMAI), phenethylammonium iodide (PEAI), and 4-fluorobenzylammonium iodide (FPMAI),[17] and (e) electron density distribution of FPMA ions (positive: green, and negative: yellow), and Bader charge with and without fluorine. (Reproduced from ref. 17 with permission from John Wiley and Sons.)[17]

Organic-ammonium halide additives can affect the mechanical properties of MHPs.[17] Bulky organic additives increased the fracture energy (cohesion energy G_c) of a perovskite thin film over G_c without the additives. A long alkyl chain (dodecylammonium iodide, DDAI) in the additive molecule yielded a larger increase in G_c (1.6 J m^{-2}) than did a short alkyl chain (butylammonium iodide, BAI) (0.87 J m^{-2}) (Fig. 2d).[17] The improved mechanical stability with the long alkyl chain additive was attributed to increased binding energy during stretching, compared to the short alkyl chain, so the former possesses higher G_c and larger plastic energy dissipation than the latter. Fluorination of an aromatic additive (4-fluorobenzylammonium iodide, FPMAI) also improved the film's mechanical stability (1.1 J m^{-2}) relative to that without fluorination (phenethylammonium iodide, PEAI) (0.75 J m^{-2}) (Fig. 2d).[17] Fluorination gives a higher binding energy between the fluorinated additive (FPMAI) and the perovskite surface (−4.33 eV) compared to PMAI (−4.28 eV), due to the high electronegativity of fluorine and concomitant increase in the mechanical fracture energy (Fig. 2e).[17]

2.2. B–X bonding

In MHPs, the mechanical properties are more affected by the inorganic framework of the halide and metal ions than by the A-site cations. The bonding strength and the flexibility of metal–halide (B–X) bonding have an important influence on the B–X framework's mechanical stiffness, so the electronegativity of the halide is also an important factor. The halide ions used in MHPs have electronegativity that decreases in the order $Cl > Br > I$; the differences affect the Pb–X bonding strengths and the resultant Young's modulus E.

The halide ions (X = I, Br, and Cl) affect the mechanical properties of $MAPbX_3$ perovskite single crystals.[14] The measured Young's modulus ranged from 10 to 20 GPa in the order of $E_{Cl} > E_{Br} > E_I$ as expected from the electronegativities of the halide component (Fig. 3a and b). First-principles DFT calculations with $MABX_3$ (B = Pb, Sn; X = Br, I) reached the same conclusion that the type and strength of B–X bonding mostly determine the elastic properties of MHPs. The bromide perovskites had higher E than did iodide, and the tin perovskites had larger E than the lead perovskites; the differences were results of the different bonding characteristics of the B–X combinations.[9]

The B–X bonding also affects the mechanical properties of $FAPbX_3$ perovskites.[14] As the electronegativity decreases, the bonding strength deceases and as a result the mechanical stiffness weakens. Also, the relatively large FA cation also causes an increase in the length of the B–X bond, and thereby degrades the inorganic framework's rigidity (Fig. 3b).[14]

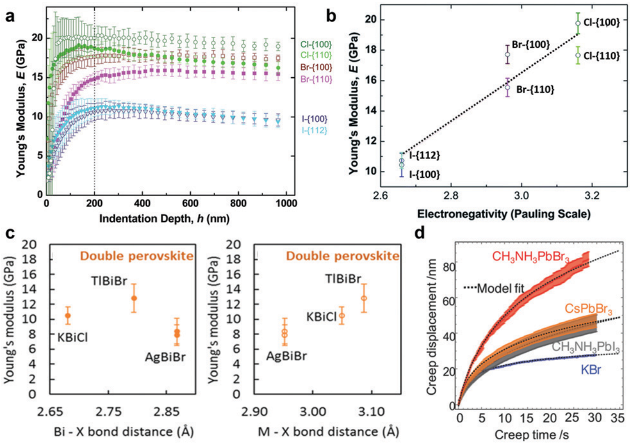

Fig. 3 Average Young's modulus of MA-based MHPs (a) with various halides (Cl, Br, and I), and (b) as a function of electronegativity, which affects the bonding strength,[14] (c) Young's modulus of lead-free MA-based metal halide double perovskites (KBiCl, TlBiBr, and AgBiBr),[13] (Reproduced from ref. 13 with permission from John Wiley and Sons.) and (d) creep displacement curves for $MAPbBr_3$, $CsPbBr_3$, and $MAPbI_3$.[16] (Reproduced from ref. 16 with permission from John Wiley and Sons.)

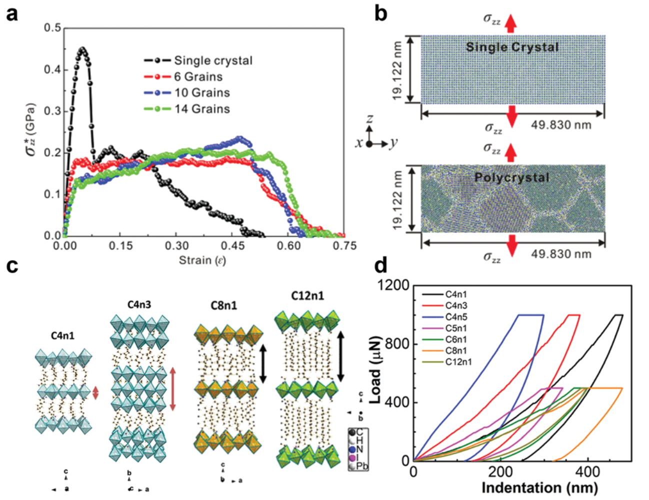

Fig. 4 (a) Stress–strain curves, (b) Poisson effect in single- and polycrystals against tensile loading,[15] (Reproduced from ref. 15 with permission from American Chemical Society.) (c) schematics of layered perovskite family $(CH_3{-}CH_2{-}CH_2{-}CH_2{-}NH_3)_2(CH_3{-}NH_3)_{n-1}Pb_nI_{3n+1}$, and (d) load–indentation curves for layered perovskites.[21] (Reproduced from ref. 21 with permission from American Chemical Society.)

Double perovskites (A_2MBiX_6, M: monovalent cation) also have interesting mechanical properties.[13,20] In a double perovskite in which trivalent Bi^{3+} and monovalent cations replace the Pb^{2+} in the single perovskite (ABX_3), the smaller bonding strength between the monovalent metal ion and halide (than between Pb^{2+} and the halide) weakens the inorganic framework against external stress, so the metal ion replacement weakens the double perovskite's mechanical stiffness (Fig. 3c).[13]

MHPs can undergo creep and stress relaxation; the Pb–X stiffness has a major influence on a MHP's dynamic mechanical responses under stress.[16] $MAPbI_3$ showed lower creep displacement than $MAPbBr_3$, because $MAPbI_3$ slipped less than $MAPbBr_3$ (Fig. 3d).

The mechanical properties of MHPs are also affected by the configuration and geometrical shapes of the X-linkers.[13] Distortion of the M–X–M bond also affects the perovskite's mechanical rigidity. $MAPbI_3$ is tetragonal and $FAPbI_3$ is cubic; their Pb–I bonding lengths are similar, but their Pb–I–Pb bonding angles differ. The PbI_6 octahedra tilt in $MAPbI_3$, so the angles of the M–I–M bonding are deflected from 180°, so elastic deformation along the $\langle 100 \rangle$ direction is easy, and the tetragonal structure leads to densely-packed structures in the perovskite crystal.

2.3. Polycrystalline thin film applications

MHPs have excellent optoelectronic properties, and therefore have been mostly used in optoelectronic devices such as photovoltaics and LEDs. Therefore, the polycrystalline thin film form of MHPs, which has abundant grain boundaries and intrinsic defects, has potential uses in flexible and stretchable perovskite optoelectronics.

Molecular dynamics simulations of the micro-structural behaviors of a $MAPbI_3$ thin film[15] showed that the single-crystalline perovskite has even more stiffness and higher tensile strength than the polycrystalline perovskite (Fig. 4a). However, polycrystalline perovskites are much more nanoductile and fracture-resistant than single crystals, mainly due to substantial amorphization of polycrystals. Due to the amorphous grain boundaries in MHP polycrystalline films, polycrystalline perovskites showed the inverse Hall–Petch relation, in which the yield stress decreases as the grain size decreases.

Two-dimensional (2D) MHPs (Ruddlesden–Popper phase) have better chemical stability than three-dimensional perovskites. 2D perovskites are composed of alternating organic and inorganic layers, and each organic layer has weak van der Waals interactions. 2D MHPs in which n in $(R\text{-}NH_3)_2MA_{n-1}Pb_nI_{3n+1}$ is low, and that have few inorganic layers, exhibited easy slipping between layers that interact by van der Waals bonding, so these perovskites have ductile properties, whereas high n increases both the out-of-plane Young's modulus and hardness.[21] In these 2D perovskites, the mechanical properties are affected more by the organic components and their weak interaction than by the B–X bonding of the inorganic framework, in contrast to 3D perovskites. Similarly, the increase in the length of the alkyl chain length reduces the Young's modulus of 2D perovskites (Fig. 4b–d).[21]

The deposition techniques and charge transport interlayers (selective contacts) also affect the mechanical fracture resistance of optoelectronic devices.[19] The methods to deposit perovskite films are crucial to determine their mechanical stability. An increased grain size of polycrystalline perovskite films also increases G_c because the grain boundaries trigger crack initiation and propagation, and thereby reduce resistance against mechanical fracture. In PSCs, the resistance to mechanical failure strongly depends on the selection of interfacial contacts; the charge-transport interfacial layers are the most fragile component in the device architecture. Also, moisture

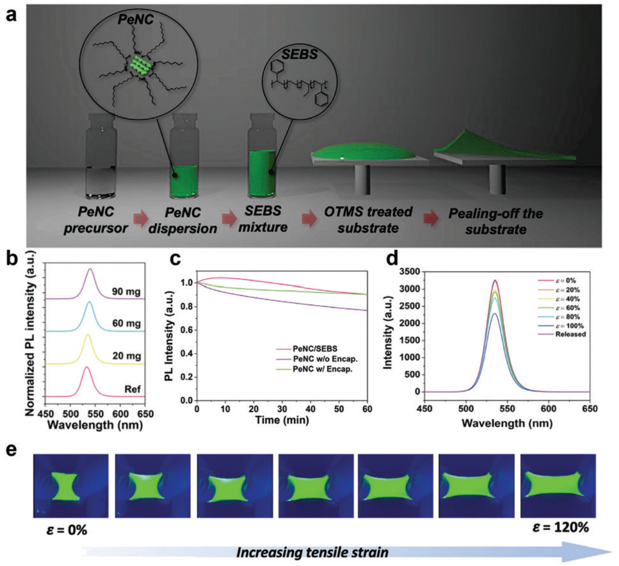

Fig. 5 (a) Schematic illustration of stretchable color-conversion-layer fabrication, (b) PL spectra according to addition of perovskite nanocrystals in a SEBS matrix, (c) PL stability of the color-conversion-layer with and without encapsulation, and (d) PL spectra and (e) optical images of the stretchable color-conversion-layer according to the uniaxial tensile strain.[18] (Reproduced from ref. 18 with permission from John Wiley and Sons.)

significantly decreases the fracture resistance of perovskite films by reducing the adhesion between the interlayers and perovskite absorbers.

The strategy to form a composite of polymer–perovskite nanocrystals can also increase the mechanical stability for stretchable applications. For this purpose, nanocrystals have been embedded into a thermoplastic polymer matrix that has a low melting temperature and is easily deformed.[22–24] The polymer matrix affects the mechanical properties of the composite materials but also increases the luminescent properties and environmental stability of the nanocrystals because they are encapsulated by the polymers.[22–24]

Stretchable color-conversion layers that incorporate perovskite nanocrystals have been developed for use in stretchable devices[18] (Fig. 5). Perovskite nanocrystals ($MAPbBr_3$) were combined with an elastic polymer (styrene–ethylene–butylene–styrene, SEBS) matrix. The composite color-conversion-layer tolerated up to 180% tensile strain. Also, the air-stability of these perovskite nanocrystals was greatly increased by encapsulating them in the elastomer matrix. Immersion of the layer in water oxidized Pb atoms that quench excitons, and decreased the incidence of defective perovskite platelets after the recrystallization of perovskite nanocrystals.

3. Engineering of flexible/stretchable electrodes

We categorize the electronic and mechanical criteria of flexible and stretchable electrodes for perovskite optoelectronics (Table 1). To be feasible replacements of conventional conducting electrodes (*e.g.*, ITO), the flexible and stretchable electrodes must have sheet resistance $\leq 100\ \Omega \text{sq}^{-1}$ and transparency $\geq$90% at a wavelength of 550 nm. They must have a reasonable pay-back time which is the operational time required to generate an amount of energy (electric or photonic) to repay the energy consumed during fabrication.[25] The flexible and stretchable electrodes must also be resilient and robust to reduce the energy pay-back time of flexible and stretchable perovskite optoelectronics, under certain bending or stretching conditions. Previous reports identified three strong candidates (*i.e.*, conducting polymers, low-dimensional carbons, and structured metals) that can achieve a good flexible electrode for perovskite optoelectronics. The properties of the materials and optoelectronic applications of these candidates are reviewed in Sections 3.

3.1 Conducting polymer electrodes

Conducting polymers can achieve a good electrode for a stretchable device with an industry-compatible fabrication process.

To modify the mechanical and electronic properties of conducting polymers, additives (*e.g.*, polar solvents, water-soluble polymers, ionic liquids, strong acids, elastomers and interfacial polymers) can be used (Fig. 6). A stretchable conducting polymer

Table 1 Criteria and estimations of flexible and stretchable electrode materials for perovskite optoelectronics

	Conductivity	Transparency	Resilience	Processability
Conducting polymer	Good[a]	Good[b]	Good for flexibility and stretchability[c]	Highly applicable to industry[d]
Low dimensional carbons	Good[e]	Good[f]	Good for flexibility[g]	Applicable to industry (graphene, CNTs)[h]
Metal wire/mesh	Very good[i]	Poor with metal substrates, good with Ag NWs and meshes[j]	Poor with metal oxides, good for flexibility with thin metal filmsand metal NWs[k]	Applicable (metal NWs or meshes),[l] and inapplicable (metal oxides and metal fibers) to industry

[a] PEDOT:PSS with H_2SO_4, ethanol, EG, and Zonyl® 4800 S cm^{-1}.[26] [b] PEDOT:PSS electrode with Zonyl® (97% at 550 nm[27]). [c] 2000 bending cycles with r_B = 4 mm,[28] 5000 stretching cycles with 10% strain,[27] 1000 stretching cycles with 70% strain,[29] 50% tensile strain with 1280 S cm^{-1}.[30] [d] Solution process, large-area casting. [e] Graphene (>200 Ω sq^{-1} (ref. 31)), CNTs (6600 S cm^{-1}).[32] [f] Graphene (97.7%).[33] [g] Graphene and CNTs (14% degradation after 2000 bending cycles with r_B = 4 mm[34]). [h] Large-area synthesis by CVD. [i] Ag mesh (4104 S cm^{-1} (ref. 35)) 10–15 Ω sq^{-1}.[36–40] [j] Ag nanowires (Ag NWs) (90% at 550 nm with 20 Ω sq^{-1} (ref. 41)), Ag mesh (96% with 4104 S cm^{-1} (ref. 35)). [k] Ti foil/mp-TiO_2 (7% degradation after 200 bending cycles, but r_B was 50 mm[42]), Ag NWs (stable after 100 cycles of bending with r_B = ~10 mm,[43] stable after 1000 stretch–release cycles to 20% tensile strain[41]), Ag mesh (95% of its original PCE after 5000 bending cycles with r_B = 5 mm, whereas that with PET/ITO dropped severely after 100 bending cycles[35]). [l] Solution process, large-area casting.

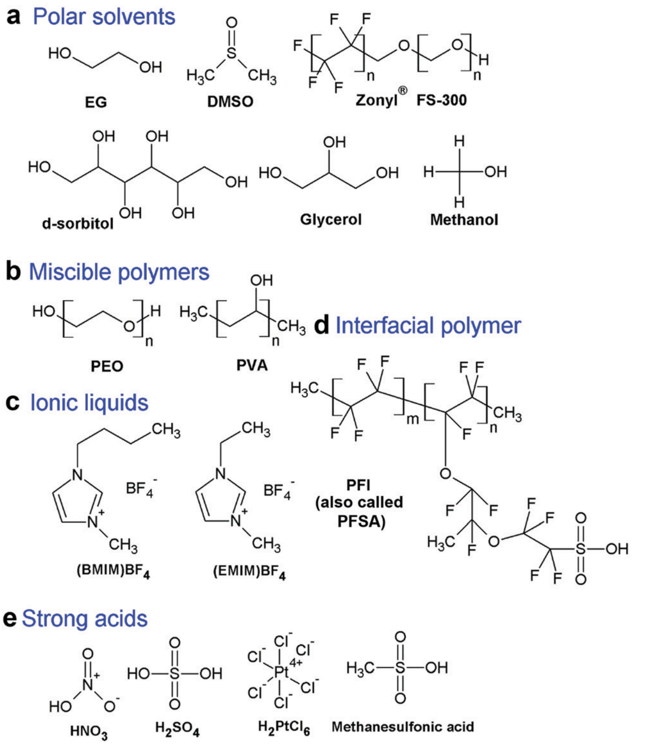

Fig. 6 Molecular structures of additives for modification of the mechanical and electronic properties of conducting polymer electrodes.

electrode with poly(3,4-ethylenedioxythiophene) (PEDOT) and poly(styrenesulfonate) (PSS) has been achieved by several molecular mixing approaches using additives such as a water-soluble polymer,[29,44] ionic liquids,[30,45–47] elastic matrix materials (*e.g.* elastomer),[28,48,49] and combinations of these approaches. A conducting polymer that has high electrical conductivity has been achieved by separating PSS grains to form interconnected PEDOT chains by using ionic liquids or strong acids, and by increasing the cohesion between PEDOT and PSS by using a polar solvent. A conducting polymer with superior charge transfer has been achieved by energy-level tuning at the interface by using interface engineering materials.[1,2,50] Thus the working mechanisms of conductive polymers with additives can be categorized according to their mechanical, electronic, and interfacial properties of PEDOT:PSS to form a flexible and stretchable electrode for perovskite optoelectronics.

PEDOT:PSS is widely used as a conducting polymer for flexible or stretchable transparent electrodes. PEDOT:PSS has been modified to yield desirable physical properties such as high optical transmittance in the visible range, high electrical conductivity, a tunable work function, high flexibility, and stretchability. PEDOT is generally oxidized, and then stabilized by PSS to achieve high conductivity and water dispersability. Thus, different types of PEDOT:PSS have been developed as hole-transport layers (*e.g.* Clevios P VP AI4083, and Clevios PH) or conductive and stretchable electrodes (*e.g.* Clevios PH500, Clevios PH510, and Clevios PH1000) depending on the molecular compositions and conformations of PEDOT and PSS. Moreover, the flexibility, stretchability, electrical conductivity, and interfacial charge transfer of PEDOT:PSS can be widely tuned to achieve flexible and stretchable optoelectronic electronics.

3.1.1. Mechanical properties. PEDOT:PSS electrodes show flexible and stretchable characteristics; these mechanical properties are superior to those of brittle inorganic interfacial materials for use in flexible and stretchable PSCs. PSCs with a PEDOT:PSS electrode on a polyethylene terephthalate (PET) substrate show good mechanical stability.[28] PEDOT:PSS electrodes showed a negligible increase in sheet resistance R_S or degradation in the power conversion efficiency (PCE) after being bent 2000 times to a bending radius $r_B = 4$ mm, whereas a perovskite solar cell with an inorganic metal oxide (In_2O_3) on PET showed obvious cracks and severe degradation of the PCE.[28] Although the PCE of the $CH_3NH_3PbI_3$ device dropped rapidly during the first several bending cycles, the PCE of the device with the PEDOT:PSS electrode then stabilized compared to that with the metalized indium oxide electrode (Fig. 7a).[28]

In addition, PET/PEDOT:PSS is an all-carbon-based substrate and electrode material, so it weighs much less than inorganic electrodes or flexible metal substrates. PSCs that use a PET/PEDOT:PSS electrode and polyurethane encapsulation showed higher power-per-weight than other organic or inorganic solar cells. Therefore, PET/PEDOT:PSS based solar cells are suitable for use as an energy source for solar-powered aircraft (Fig. 7b).[51]

An as-cast pristine PEDOT:PSS film has relatively poor elasticity (∼2% elongation at break), so various methods have been evaluated to increase it. Deposition of conducting polymers within geometrically wavy patterns or on prestrained (buckled) elastomeric substrates increased the stretchability but seems unlikely to achieve a flexible and stretchable device within a planar area in the device (Fig. 7c).[27]

Another strategy is to embed the conducting polymer in an insulating elastomeric matrix such as polyurethane (PU) or PDMS. A blend of PEDOT:*p*-tosylate with an aliphatic PU elastomer achieved a highly stretchable conducting electrode that had a conductivity of 120 S cm^{-1} (Fig. 7d).[48] A composite of PEDOT:PSS and PDMS is flexible, stretchable, and stable; it remains elastic under reversible compressive stress ($\varepsilon = 60\%$) and strain stress ($\varepsilon = 43\%$), and retained low R_S without a detectable change even after 5000 cycles of complete folding (Fig. 7e).[49] However, the elastomer is an insulator, so the conductivity of the composite is limited.

Zonyl® fluorosurfactant plasticizes PEDOT:PSS by decreasing its tensile modulus and increasing its crack-onset strain. Zonyl® also increases the surface wettability and conductivity of the stretchable conducting polymer electrode. A PEDOT:PSS electrode with Zonyl® is highly conductive ($R_S = 240\ \Omega\ q^{-1}$) and transparent (optical transmittance = 97% at 550 nm), and can withstand over 5000 stretching cycles of 10% strain with no change in R_S.[27]

Water-soluble polymers with PEDOT:PSS can simultaneously increase the stretchability and conductivity of an electrode.[29,44] They have good miscibility with PEDOT:PSS, so the Coulombic interaction between PEDOT and PSS is screened

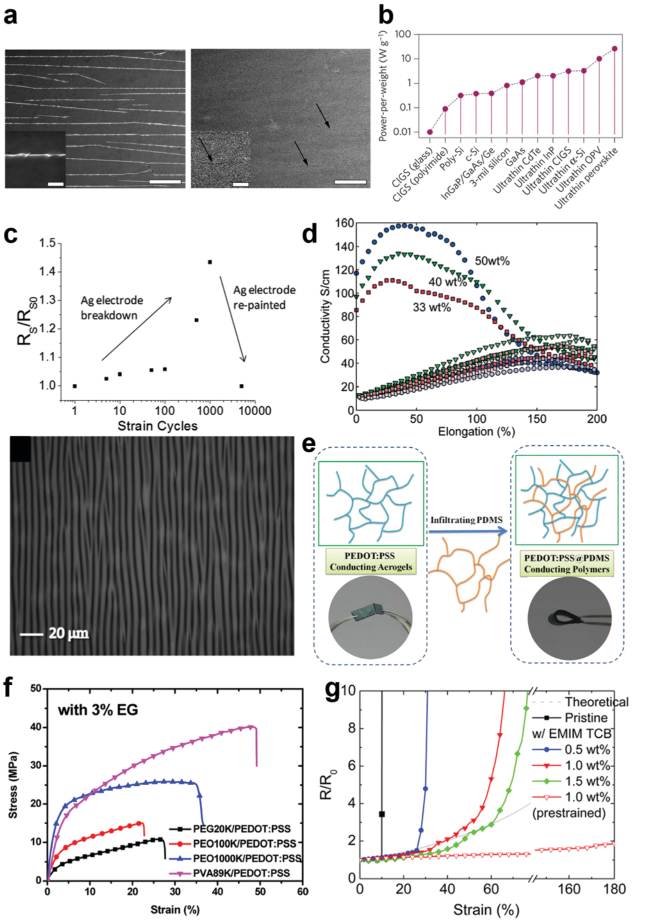

Fig. 7 (a) SEM images of the perovskite film on PET/M-In_2O_3 (left) and PET/HC-PEDOT/SC-PEDOT (right) after 2000 bending cycles,[28] (b) schematic structure and power-per-weight of an ultrathin perovskite solar cell,[51] (Reproduced from ref. 51 with permission from Springer Nature.) (c) normalized sheet resistance *versus* stretching cycles (10% strain) and optical microscopy image (0% strain) of a buckled PEDOT:PSS film with 1 wt% Zonyl®,[27] (Reproduced from ref. 27 with permission from John Wiley and Sons.) (d) conductivity *versus* elongation of PEDOT (200% strain),[48] (Reproduced from ref. 48 with permission from John Wiley and Sons.) (e) schematic of PEDOT:PSS with polydimethylsiloxane (PDMS) conducting polymers,[49] (f) stress–strain curves of free-standing PEDOT:PSS with water-soluble polymers,[44] (Reproduced from ref. 44 with permission from American Chemical Society.) and (g) normalized sheet resistances of PEDOT:PSS films with EMIM TCB.[30] (Reproduced from ref. 30 with permission from American Chemical Society.)

by the water-soluble polymers (*e.g.* poly(ethylene oxide) (PEO), and poly(vinyl alcohol) (PVA)). This screening effect induces phase segregation of PSSH from PEDOT:PSS; as a result the conformation of PEDOT chains changes from coiled to extended. Therefore, the water-soluble polymer and PEDOT:PSS blended film shows both high stretchability and high conductivity.[44] The blended film increased the elongation-at-break from 2% to 55% and the conductivity from 0.2 to 75 S cm^{-1} depending on the molecular weight and the mixing ratio of the polymers (Fig. 7f).[44]

Ionic liquid, 1-ethyl-3-methylimidazolium:tetracyanoborate (EMIM:TCB, 1.3 wt%), can be used to achieve high stretchability and conductivity of conducting polymers.[30] EMIM:TCB mixed with PEDOT:PSS yields high stretchability (50% tensile strain) and high conductivity (1280 S cm^{-1}) simultaneously. EMIM:TCB is used as a secondary dopant (*e.g.*, polar solvent, surfactant, or ionic liquid) to induce a structural transformation of PEDOT:PSS and increase its conductivity as well as a plasticizer that increases the free volume of PEDOT:PSS to make it stretchable (Fig. 7g).[30]

3.1.2. Electrical conductivity.

The direct-current electrical conductivity of an electrode composed of an as-cast undoped PEDOT:PSS film is 0.08–0.76 S cm^{-1} depending on the PEDOT-to-PSS ratio.[52] However, the conductivity of doped PEDOT:PSS has been significantly improved to >4000 S cm^{-1} by using various dopants such as polar solvents, strong acids, or ionic liquids.[26] To increase the conductivity of stretchable conducting polymer electrodes, the content of insulating components must be decreased. Most methods to achieve this goal include blending the conducting polymer and additives without an elastomeric matrix. The key is an extended conductive PEDOT:PSS domain caused by a formation of highly-oriented PEDOT chains and a depletion of insulating PSS. Compared to the aggregated grains of PEDOT and PSS in pristine films, the dopants remarkably improve the π–π stacking of ordered PEDOT chains in the extended PEDOT:PSS domains, so the conductivity of the electrode is highly increased.

Polar solvents (*e.g.* DMSO, ethylene glycol (EG), glycerol, D-sorbitol, methanol, Triton™ X, and Zonyl® fluorosurfactant) have been used to increase the conductivity of PEDOT:PSS. DMSO increases the cohesion and the resulting electrical conductivity of the PEDOT:PSS film. In pristine PEDOT:PSS without DMSO, PEDOT:PSS domains consist of a PEDOT-rich core and a PSS-rich shell; the domains are held together by weak inter-PSS hydrogen bonding, so cracks propagate easily and G_c is low. Blending with DMSO forms an inter-PEDOT bridge, and expands the PEDOT:PSS grains because the PSS-rich shell is dissolved by the polar groups (SO and SCH_3) of DMSO. Therefore, addition of 3 wt% DMSO to PEDOT:PSS increases the cohesion by 4.7 times and the electrical conductivity by 60.5 times (Fig. 8a).[53] In the same manner, an expanded PEDOT chain with a coiled conformation is formed by mixing with EG, so the conductivity of the film was increased to 160 S cm^{-1}.[54] The conductivity can be further increased (1418 S cm^{-1}) by immersing PEDOT:PSS films in EG baths. The insulating PSS molecules at the surface are removed by EG, and then the PEDOT chain elongates (Fig. 8b).[55]

Ionic liquids (*e.g.* 1-butyl-3-methyl imidazolium tetrafluoroborate $(BMIM)BF_4$, or 1-ethyl-3-methylimidazolium tetracyanoborate (EMIM)TCB) can simultaneously yield high stretchability and conductivity of PEDOT:PSS films. Ionic liquids are classified as organic/inorganic salts; for instance, (EMIM)TCB consists of cations (*i.e.* imidazolium) which induce the lowest viscosities and highest conductivities, and small anions with delocalized charges (*i.e.* TCB) which increase the conductivity of ionic liquids.[57] The PSS domains are swollen by the ionic liquid, and then the merged PEDOT grains and excess PSS grains separate to form interconnected PEDOT chains, which increase the conductivity of the film (136 S cm^{-1} with

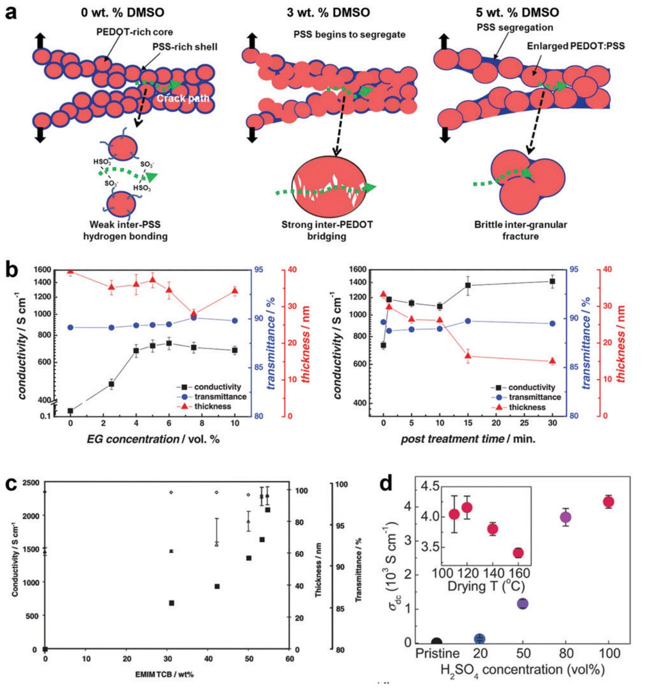

Fig. 8 (a) Schematics of the debonding mechanism of PEDOT:PSS after mixing with dimethyl sulfoxide (DMSO),[53] (Reproduced from ref. 53 with permission from American Chemical Society.) (b) conductivity, transmittance and film thickness of PEDOT:PSS with ethylene glycol (EG) blending and the solvent post-treatment time,[55] (Reproduced from ref. 55 with permission from John Wiley and Sons.) (c) conductivity (square), film thickness (triangle), and transmittance (diamond) variations *versus* concentration of 1-ethyl-3-methylimidazolium tetracyanoborate (EMIM TCB) in solution,[46] (Reproduced from ref. 46 with permission from John Wiley and Sons.) and (d) conductivities of PEDOT:PSS films with various concentrations of H_2SO_4.[56] (Reproduced from ref. 56 with permission from John Wiley and Sons.)

60 wt% $(BMIM)BF_4$). The dimension of phase-separated PEDOT:PSS by the ionic liquid is about 40–60 nm; this dimension may be related to the critical thickness (107 nm) that must be achieved to increase the conductivity of PEDOT:PSS by the $(BMIM)BF_4$ ionic liquid.[46] The conductivity of doped PEDOT:PSS is up to 2084 S cm^{-1} using (EMIM)TCB, and up to 287 S cm^{-1} using $(BMIM)BF_4$; both far exceed the conductivity of undoped PEDOT:PSS (0.68 S cm^{-1}) (Fig. 8c). In the pristine PEDOT:PSS film, the PEDOT domains are small and disconnected; blending with (EMIM)TCB transforms them to large and interconnected domains.

A strong acid can increase the conductivity of PEDOT:PSS. As-cast PEDOT:PSS films are soaked in highly concentrated strong acids or high-temperature (120–160 °C) diluted acid aqueous solution.[56] Hydrogen ions (H^+) from the acid (*e.g.* H_2SO_4, HNO_3, and H_2PtCl_6) react with sulfuric ions (PSS^-) in PEDOT:PSS to form neutral PSSH. PEDOT and neutral PSSH are unlikely to interact by Coulombic attraction, so the PSSH chains separate from the PEDOT:PSS complex. Rinsing the film with deionized water can remove the PSSH. As a result, the remaining PEDOT:PSS segregates into a phase that is rich in PEDOT, with a minimal amount of PSS; this process greatly increases the conductivity. Treatment of PEDOT:PSS with strong H_2SO_4 significantly increases its conductivity (4380 S cm^{-1}). After soaking PEDOT:PSS in 100% H_2SO_4 and then washing with deionized water, the strong π–π stacking nature and the rigidity of PEDOT induce formation of crystalline nanofibril structures in PEDOT:PSS; the insulating and hygroscopic PSS is noticeably removed (Fig. 8d). To prepare high-quality conducting polymer films on a plastic substrate, a mild acid (*e.g.*, methanesulfonic acid MSA) is used instead of corrosive H_2SO_4 and combined with treatment using ethanol, EG and Zonyl® to achieve a conductivity of 4800 S cm^{-1}.[26] The optimized PEDOT:PSS films retained about 14.6% of their initial conductivity after the film was bent 100 times in an ambient atmosphere.

3.1.3. Interface engineering.

The mechanical and electrical properties of flexible and stretchable perovskite optoelectronics are considerably affected by a coupling effect at the interface between the electrode and perovskite films. At this interface, suppression of defect diffusion improves the stability, and the decrease of the energy-level offset increases the charge transfer in the devices. Additives such as DMSO, sorbitol, and MSA tend to decrease the work function (WF) of PEDOT:PSS,[26] because the treatment decreases the PSS-to-PEDOT ratio at the film surface. PEDOT:PSS blend films with 3, 7, and 11% DMSO showed a ∼0.1 eV decrease in the WF, and a decreased PSS/PEDOT ratio at the surface.[58] Moreover, PEDOT:PSS blend films with 2, 5, and 10 wt% sorbitol showed a ∼0.3 eV decrease in the WF. Acid treatment can also decrease the WF of PEDOT:PSS electrodes. Acid modification using MSA decreased the WF of PEDOT:PSS electrodes from −5.0 to −4.8 eV. These decreases in the WF of PEDOT:PSS are consistent with the reduction of PSS molecules at the surface.

The valence band maxima (VBMs) of perovskites are about 5.4–5.9 eV depending the component atoms and structures, whereas the WF of unmodified or untreated PEDOT:PSS is about 4.8–5.4 eV depending on the surface composition.[59] Therefore, in p–i–n structured perovskite optoelectronics, the treatments to increase the conductivity of PEDOT:PSS also increase the energy-level offset between the treated conducting polymer electrode and the perovskite, and cause poor charge injection between the perovskite and polymeric electrode in PeLEDs and decrease of built-in potential in PSCs. To overcome this problem, interface engineering must be applied to control the energy level of the conducting polymer.

In p–i–n PSCs, the WF of flexible conducting polymeric electrodes must be increased to reduce the energy-level offset between the WF of PEDOT:PSS and the VBM of the perovskite. Thus, polymeric additives are used to increase the WF of films. A perfluorinated ionomer (PFI) blended with PEDOT:PSS achieves a high WF, and increased charge injection in PeLEDs and V_{OC} in PSCs.[1,2,60,61] The difference in the surface energies of PEDOT:PSS and PFI tends to enrich the PFI on the film surface, so the WF of PFI-blended PEDOT:PSS at the interface with the perovskite can be tuned by adjusting the mixing ratio of PFI to PEDOT:PSS. As a result, the tuned WFs of PFI blended PEDOT:PSS are well aligned with the VBMs of various photoactive perovskites ($MAPbI_3$, $MAPbBr_3$, $MAPbBr_3$ nanocrystals,

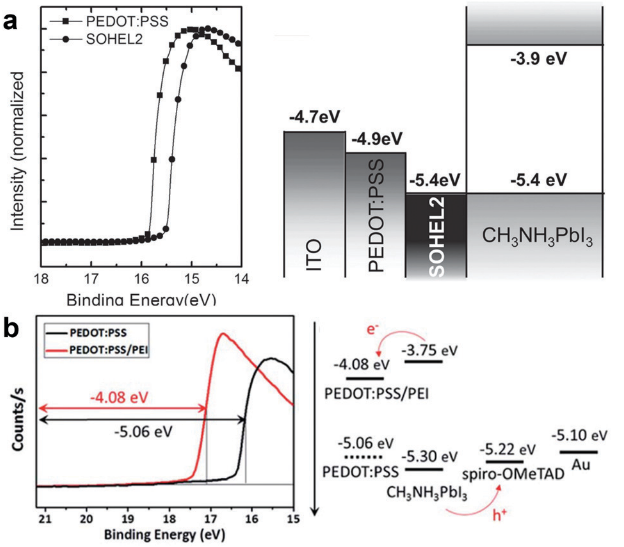

Fig. 9 Photoemission cutoffs obtained by UPS and energy level diagrams of work function tuned PEDOT:PSS with (a) a perfluorinated ionomer (PFI) for the p–i–n device[62] (Reproduced from ref. 62 with permission from John Wiley and Sons.) and (b) polyetherimide (PEI) for the n–i–p device.[50]

$CsBr:PbBr_2$, and $CsPbBr_3$) and thereby allow quasi-Ohmic contact at the interface (Fig. 9a).

In n–i–p PSCs, the WF of flexible conducting polymeric electrodes must be decreased to facilitate electron transport between the conducting polymeric electrodes and the conduction band maximum (CBM) of the perovskites. Spin-coating of polyetherimide (PEI) onto the surface of the PEDOT:PSS electrode decreases its WF from −5.06 to −4.08 eV. The change occurs because a dipolar PEI thin film creates a surface dipole moment at the interface of PEDOT:PSS and the perovskite. The CBM of $MAPbI_3$ is −3.75 eV, so the reduced WF of the polymeric electrode is suitable for electron transport in the device (Fig. 9b).[50]

Interface engineering is widely utilized for not only energy level alignment but also defect passivation and a permeation barrier. The defects at the interface between the perovskite and charge transfer layer are an active carrier recombination site. Carrier recombination greatly reduces J_{SC} and the PCE of PSCs, and therefore interface engineering for defect passivation is employed to reduce the carrier recombination in PSCs. Organic interfacial layers are also utilized for defect passivation. A rhodamine layer passivated the surface trap states at the PCBM layer in PSCs, and thus nonradiative recombination and band bending at the interface were reduced to enhance the charge transfer.[63] A triblock-functionalized fullerene derivative (PCBB–2CN–2C8) was used to passivate the surface trap states at the TiO_2 layer in PSCs. Because of the rapid degradation of the TiO_2/perovskite interface due to O_2 release of TiO_2 under UV irradiation, the defect passivation of the PCBB–2CN–2C8 interfacial layer enhanced the charge transfer and reduced the hysteresis and operational degradation.[64] 4-(1,3-dimethyl-2,3-dihydro-1*H*-benzimidazol-2-yl)-*N*,*N*-diphenylaniline (*N*-DPBI) which doped C_{60} was employed to fill the trap states at the C_{60}/perovskite interface and reduce the interfacial trap density.[65]

Interfacial engineering is also employed for preventing permeation of water, oxygen, ions and metallic species to retard the degradation of flexible perovskite optoelectronics. The multiple degradation processes with molecular permeation through the interface (*e.g.*, decomposed organic cations in the perovskite (*e.g.*, MA^+ and FA^+), generated inorganic byproducts in the perovskite (*e.g.*, PbI_2 and metallic Pb), migration of electrode components (*e.g.*, Sn, In, Al, and Ag) into the perovskites, and migration of ions (anions and cations) from the perovskites) are effectively blocked by interfacial materials with physical robustness (*e.g.*, $N^2,N^{2\prime},N^7,N^{7\prime}$-tetrakis(9,9-dimethyl-9*H*-fluoren-2-yl)-$N^2,N^{2\prime},N^7,N^{7\prime}$-tetrakis(4-methoxyphenyl)-9,9′-spirobi[fluorene]-2,2′,7,7′-tetraamine (DM),[66] polyethyleneimine (PEI),[67] CuPc,[68] and rGO:PCBM) or chemical inactivation (*e.g.*, PFI,[1] 9-(2-ethylhexyl)-*N*,*N*,*N*,*N*-tetrakis(4-methoxyphenyl)-9*H*-carbazole-2,7-diamine (EH44),[69] and C_{60}-SAM[70]). Then, the degradation in flexible and stretchable perovskite optoelectronics is efficiently suppressed by interface engineering. As a result, the operational stability of PSCs is significantly increased with interfacial layers.[25]

3.1.4. Optoelectronic applications. PEDOT:PSS films blended with various additives are used in PSCs and PeLEDs to form light-weight, highly-conductive and flexible polymeric electrodes. The devices have a variety of structures and properties (Tables 3 and 4).

Light (23 W g^{-1}), flexible, and ultrathin (3 μm) PSCs use a polymer substrate and a highly-conductive PEDOT:PSS layer (PH1000) blended with DMSO and Zonyl®.[51] This blended conductive polymer layer is a transparent, conductive ($R_S \sim$ 105 Ωsq^{-1}), oxide-free (indium tin oxide (ITO), glass) hole-selective flexible electrode that can be fabricated at low temperature (110 °C). The DMSO additive achieves pinhole-free perovskite layer formation with uniform coverage even on rough plastic substrates. The devices have short-circuit current $J_{SC} = 17.5 \pm 1$ mA cm^{-2}, open-circuit voltage $V_{OC} = 930 \pm 40$ mV and an excellent fill factor (FF) ∼80% on glass/ITO and ∼76% on polymer foil. These traits correspond to a PCE = 12.5 ± 1% for reference cells on glass and 12 ± 1% for cells on ultrathin polymer foil. Use of a Cr/Cr_2O_3 interlayer greatly increases the air stability of the ultra-thin and light PSCs (Fig. 10a).[51]

Highly-conductive PEDOT:PSS (PH1000) modified with EG has been used as a semitransparent flexible anode to obtain an inexpensive TCO-free flexible perovskite planar-heterojunction solar cell that can be fabricated at low temperature by spray-coating PEDOT:PSS PH1000 with EG diluted in 2-propanol.[72] The optimized anode showed a low R_S = 28 Ωsq^{-1}, and high transparency (mean transmittance >60% between 300 nm and 800 nm).[72]

p–i–n PSCs have been fabricated using an interfacial layer of PEDOT:PSS (AI 4083) that has a high WF, on the surface of PEDOT:PSS that had been treated to achieve high conductivity (MSA treatment on PH1000). The double layers of PEDOT:PSS had a high conductivity of 2540 S cm^{-1} due to the MSA-induced phase segregation between PSS and PEDOT in the PEDOT:PSS

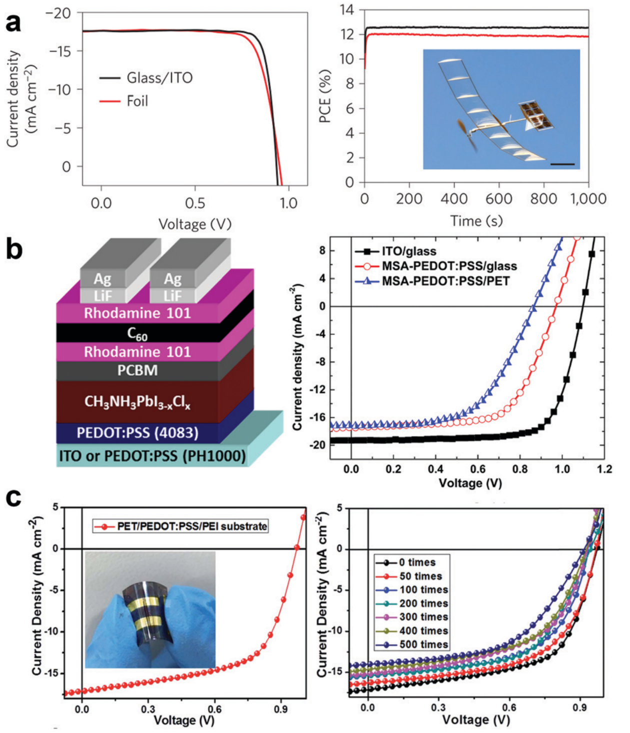

Fig. 10 Photovoltaic parameters of PSCs with conducting polymers. (a) Current density–voltage (*J*–*V*) curves and efficiency drop in ambient air of ultrathin and light perovskite solar cells under 1000 W m^{-2} simulated solar illumination (inset: photograph of a solar-powered model airplane with ultrathin and light PSCs),[51] (Reproduced from ref. 51 with permission from Springer Nature.) (b) schematic architecture and *J*–*V* curves of p–i–n PSCs with an MSA-treated PEDOT:PSS electrode,[71] (Reproduced from ref. 71 with permission from American Chemical Society.) and (c) *J*–*V* curves of n–i–p PSCs on a PET substrate with PEDOT:PSS/PEI electrodes.[50]

film, and the coil-to-linear conformational change of the PEDOT chains. The double layers also show a WF = −4.9 eV using the PEDOT:PSS interfacial layer; this is an improvement over the reduced WF of the MSA-treated PEDOT:PSS electrode (−4.8 eV) as a result of the partial removal of PSS at the surface of the treated film. Therefore, the device with the MSA-treated PEDOT:PSS (PH1000) and PEDOT:PSS interfacial layer (AI 4083) showed a high average PCE = 10.6% on a glass substrate, and 8.1% on a flexible PET substrate.[71]

The double layers of PEDOT:PSS on PET form a flexible transparent electrode that is more resilient than TCO on PET. The PCE of the device that used PEDOT:PSS double layers tardily decreased from 7.5% to ∼5.5% even after 2000 bending cycles with r_B = 2–3 mm at a frequency of 1 Hz. However, the initial PCE of the device with the PEDOT:PSS double layers was inferior (average PCE 8.6%) compared to that of the control device with an ITO electrode (average PCE 14.7%) due to poor conductivity (2540 S cm^{-1}) than ITO (∼6000 S cm^{-1}) and low incident photon to current conversion efficiency in the ultraviolet range (Fig. 10b).[71]

PEI is used at the interface of highly-conductive PEDOT:PSS (PH1000) and MAPbI$_3$ in n–i–p PSCs. PEI has insulating properties, so the conductivity of the PEI-coated PEDOT:PSS film (2160 S cm^{-1}) is slightly lower than that of bare PEDOT:PSS (2500 S cm^{-1});[50] however, the WF of PEDOT:PSS/PEI is increased from −5.06 to −4.08 eV and is highly stable during operation. Therefore, the device with PEDOT:PSS/PEI showed a comparable PCE (12.42%) to that of the device with a metal oxide-based electrode such as fluorine-doped tin oxide (FTO)/TiO$_2$ (14.38%) or ITO/PEDOT:PSS (13.45%).[50] The device with PEDOT:PSS/PEI also has higher stability of the PCE than devices with FTO/TiO$_2$ and ITO/PEDOT:PSS. After storage for 7 d at 30–40% humidity, the degradation of the PCE was 15% in the device with PEDOT:PSS/PEI, but 22% in the device with FTO/TiO$_2$ and 27% in the device with ITO/PEDOT:PSS.[50] ITO is gradually etched during device fabrication and operation due to the acidic nature of PEDOT:PSS, and the released In and Sn ions degrade the perovskite layer. Moreover, FTO/TiO$_2$ forms reactive superoxide or deep electron traps after UV exposure, and these degrade the perovskite. However, the high stability of the PSC is a result of its use of a PEDOT:PSS/PEI layer. It reduces the film's hygroscopicity to protect the perovskite layer from moisture (Fig. 10c).[50]

High-efficiency metal halide PeLEDs were obtained using a modified conducting polymer anode.[2] The exciton quenching in a MHP emitting layer (EML) was managed by stoichiometry modification and optimized nanosized perovskite grain formation of MAPbBr$_3$. A slight increase in the ratio of MABr to PbBr$_2$ suppressed formation of metallic Pb in the EML, and thereby reduced non-radiative recombination inside the EML. Use of the nanocrystal pinning process improved the surface coverage on the conducting polymer anode. The suppressed metallic Pb formation and uniform film formation with small nanograins increased its luminescence efficiency. A self-organized conducting polymer (SOCP) anode made of highly conductive PEDOT:PSS and PFI was used as a flexible anode which acts both as an anode and a hole injection layer.[2] The SOCP develops a gradient ionization potential that increases toward the EML by self-organization of polymer chains; the surface potential reaches ∼5.80 eV. The use of the SOCP reduces the energy barrier for hole injection from PEDOT:PSS (4.8 eV) to the valence band maximum of the MAPbBr$_3$ EML (6.01 eV) and thereby increases the luminescence efficiency and luminance–voltage characteristics of green PeLEDs (current efficiency CE = ∼42.9 cd A^{-1}) (Fig. 11a–d).[2]

The ideally desired properties of a conducting polymer anode are high electrical conductivity, high WF, and reduced exciton quenching on the anode. A molecular decoupling strategy for a conducting polymer anode yielded these three properties.[6] Conventional methods to increase the electrical conductivity of conducting polymers usually reduce the WF of the polymer anode because the conventional post-treatment removes insulating surface PSS components.[73] MAI and DMSO as co-additives to PEDOT:PSS induce growth of nanofibril PEDOT-rich grains by weakening the Coulombic attraction between PEDOT and PSS (Fig. 11e), in which the resonant structure of the thiophene ring changes from benzoid to quinoid and increases its electrical conductivity by improving the π–π stacking. The molecularly-controlled polymeric anode

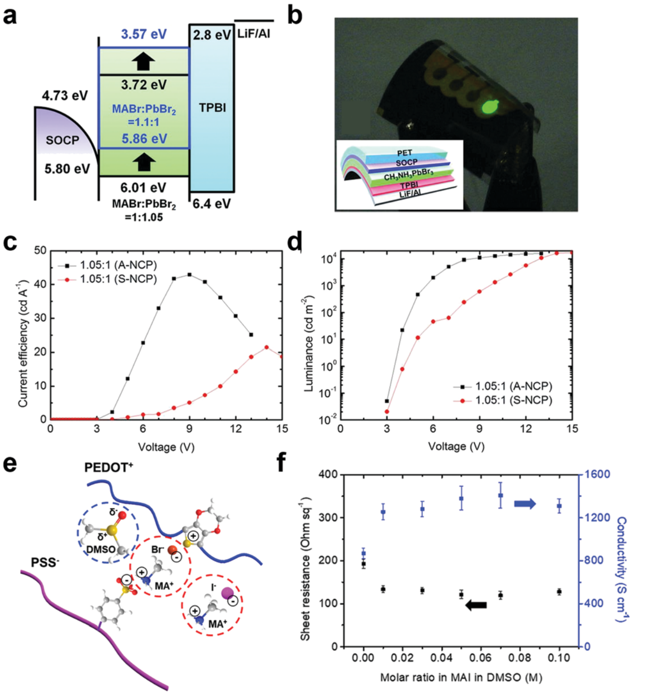

Fig. 11 (a) Energy band diagram of MAPbBr$_3$ PeLEDs with a self-organized polymeric anode, (b) optical image and schematic device structure of flexible PeLEDs, and (c) current efficiency and (d) luminance *versus* voltage of the PeLEDs.[2] (Reproduced from ref. 2 with permission from The American Association for the Advancement of Science.) (e) Schematic illustration of the weakening of the PEDOT–PSS Coulombic attraction by MABr and MAI additives, and (f) conductivity evolution of the PEDOT:PSS film according to the MABr ratio.[6] (Reproduced from ref. 6 with permission from Elsevier.)

achieved a high conductivity (~1409.47 S cm^{-1}) (Fig. 11f) and high surface WF (~5.85 eV), and the PeLEDs with the modified polymer anode had a high CE = 52.86 cd A^{-1}, and external quantum efficiency (EQE) = 10.93%.[6]

The chemical composition and polarity of the conducting polymer also affect the perovskite film differently from the crystallization of the overlying perovskite crystals and resulting film morphology of the EML. Polar solvent-soluble self-doped conducting polymers affect conventional PEDOT:PSS.[74] The conducting polymer (poly(styrenesulfonate)-grafted polyaniline (PSS-*g*-PANI)) is soluble in a polar solvent, and retards evaporation of the good solvent (*i.e.*, DMSO) for MAPbBr$_3$; this characteristics increased the controllability of perovskite crystal growth by using solvent treatment and the nanocrystal pinning process. PSS-*g*-PANI induced a granular-structure perovskite EML film, which helped to spatially confine the charge carriers inside perovskite grains and thereby increased the LED device efficiency (CE = 14.3 cd A^{-1}) compared to conventional PEDOT:PSS (CE = 7.07 cd A^{-1}).[74]

Conducting polymers have been also used as stretchable electrodes for PeLEDs. A composite polymer anode that consisted of PEDOT:PSS and poly(ethylene oxide) (PEO) has been used to fabricate a stretchable PeLED,[84] and a perovskite–polymer composite film (*i.e.*, MAPbBr$_3$–PEO) has been used as a stretchable EML to provide elastic connection between brittle perovskite crystals. Inclusion of PEO in PEDOT:PSS greatly increased the required mechanical strain to induce failure of PEDOT:PSS, and also improved its electrical conductivity by changing its resonant structure from benzoid to quinoid. Addition of 33 wt% PEO to PEDOT:PSS[44] yielded high conductivity (~35 600 S cm^{-1}) and high transmittance (82% at 550 nm). The stretchable PeLEDs showed a maximum luminance of 15 960 cd m^{-2} and maintained their initial luminous characteristics against 40% uniaxial strain (Fig. 12). The PEDOT:PSS–PEO composite anode had high mechanical resilience against stretching.[29] A polydimethylsiloxane (PDMS) substrate/PEDOT:PSS–PEO anode was formed in a buckling structure to increase the mechanical stretchability of PeLEDs. The intrinsic PEDOT:PSS was easily cracked, and failed completely under

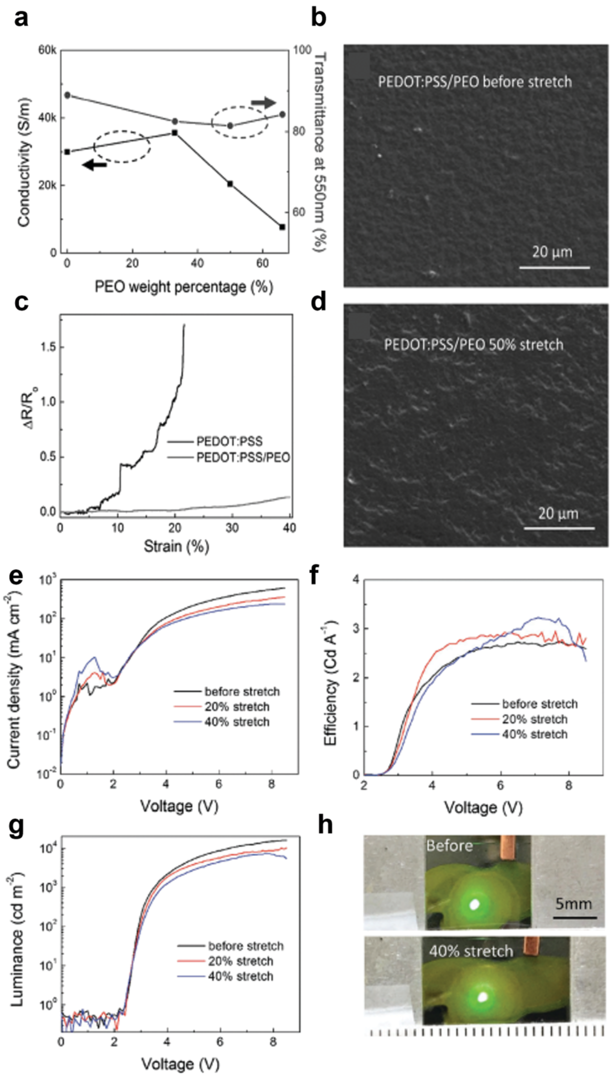

Fig. 12 (a) Conductivity and optical transmittance *versus* PEO weight percentage, (b) scanning electron microscope (SEM) image of PEDOT:PSS/PEO before stretching, (c) sheet resistance *vs.* mechanical strain, (d) SEM image of PEDOT:PSS/PEO before 50% strain, (e) current density, (f) current efficiency, and (g) luminance of stretchable LEDs *vs.* strain, and (h) optical image of stretchable LEDs before and after 40% stretching.[84] (Reproduced from ref. 84 with permission from John Wiley and Sons.)

Table 2 Electrical and mechanical properties of conducting polymers with various additives

Additives for the conducting polymer		Electrical properties	Mechanical properties
Ionic liquids	PEDOT:PSS with STEC[a] [45]	3100 S cm^{-1}	Tensile strain 100% with 1000 stretching cycles, then conductivity 3600 S cm^{-1}. Tensile strain 600%, then conductivity 600 S cm^{-1}.
	PEDOT:PSS with (EMIM)TCB[b] [30]	1280 S cm^{-1}	Tensile strain 180%, then R increased 200%
	PEDOT:PSS with (EMIM)TCB[46]	2084 S cm^{-1}	
	PEDOT:PSS with (EMIM)TCB[47]	2100 S cm^{-1}	Tensile strain 30%, then R increased ∼57%
	PEDOT:PSS with $(BMIM)BF_4$[c] [46]	287 S cm^{-1}	
Polar solvent	Zonyl® [27]	R_S = 240 Ω sq^{-1}	Tensile strain 10% with 5000 stretching cycles, then no change in R_S
	PEDOT:PSS with DMSO[d] [76]	670 S cm^{-1}	
	PEDOT:PSS with EG[e] [77]	5012 S cm^{-1}	
Strong acid	PEDOT:PSS soaked in HNO_3[78]	4100 S cm^{-1}	
	PEDOT:PSS soaked in MSA[f] [79]	3300 S cm^{-1}	
	PEDOT:PSS soaked in H_2SO_4[56]	4380 S cm^{-1}	
	P123/PEDOT:PSS treated by H_2SO_4[80]	1700 S cm^{-1}	Tensile strain 40% with 1000 stretching cycles, then R increased 4%
Elastomer	HC[g]-PEDOT/SC[h]-PEDOT on PET[28]		2000 bending cycles with r_B = 4 mm, then no change in R_S
	PEDOT:*p*-tosylate with aliphatic PU[i] [48]	120 S cm^{-1}	Tensile strain 200%, then 65% decreased conductivity
	PEDOT:PSS with PDMS[j] [49]		Compressive stress 60% and tensile stress 43% with 5000 cycles, then no change in R_S
Water-soluble polymer	PEDOT:PSS with PEO[k] [29]		1000 stretching cycles with 70% strain
	PEDOT:PSS with PVK[l] [44]	172 S cm^{-1}	Tensile strain 50%, then break-down of the free-standing film
Interface engineering materials	PEDOT:PSS with PFI[m] [1,2]	WF = −4.8 to −5.80 eV	
	PEDOT:PSS/PEI[n] [50]	WF = −5.06 to −4.08 eV	
Combinations	PEDOT:PSS with H_2SO_4, ethanol, EG, and Zonyl® [26]	4800 S cm^{-1}	
	PEDOT:PSS:MSA/PEDOT:PSS:PVA[o] [81]	3100 S cm^{-1}	Tensile strain 30% with 400 stretching cycles, then no change in R
	PEDOT:PSS with sodium dodecyl sulfate on cotton[82]	1335 S cm^{-1}	Tensile strain 80%, then R increased 262%

[a] STEC: stretchability and electrical conductivity enhancers. [b] EMIM TCB: 1-ethyl-3-methylimidazolium tetracyanoborate. [c] BMIM: 1-butyl-3-methyl imidazolium tetrafluoroborate. [d] DMSO: dimethyl sulfoxide. [e] EG: ethylene glycol. [f] MSA: methanesulfonic acid. [g] HC: higly conductive. [h] SC: semiconducting. [i] PU: polyurethane. [j] PDMS: polydimethylsiloxane. [k] PEO: poly(ethylene oxide). [l] PVK: polyvinylcarbazole. [m] PFI: perfluorinated ionomer. [n] PEI: polyetherimide. [o] PVA: poly(vinyl alcohol).

20% strain, but the composite polymer anode did not crack under 70% strain. PeLEDs fabricated using the composite anode and $MAPbBr_3$–PEO EML also maintained their device performance up to 70% tensile strain and 1000 cycles of stretching.

Section 3.1 has identified the conducting polymer electrode as one of the most promising candidates for flexible and stretchable electrodes in perovskite optoelectronics. The mechanical and electronic properties of conducting polymers are appropriate to achieve perovskite optoelectronics that have good conductivity (maximum 4800 S cm^{-1} (ref. 26)), good transparency (97% at 550 nm[27]), flexibility (2000 bending cycles with r_B = 4 mm[28]), stretchability (5000 stretching cycles with 10% strain,[27] 1000 stretching cycles at 70% strain,[29] and 50% tensile strain with 1280 S cm^{-1} (ref. 30)), and industry applicability (Table 1). Those properties of conducting polymers have been significantly improved by several types of additive engineering (Table 2), so efficient and resilient perovskite optoelectronics under bending or stretching stress are being developed (Tables 3 and 4).

3.2. Low-dimensional carbon electrodes

For electrode applications in LEDs and solar cells, carbon electrodes must have appropriate electronic and electrical properties in addition to mechanical flexibility. The electrical conductivity and work function of carbon materials directly influence the charge-injection or charge-collection efficiencies of LEDs and SCs, and thereby determine the device efficiency and stability.[31,86–91] Therefore, chemical modifications are frequently applied to carbon materials to adjust their sheet resistance and work function, so the environmental stability of chemically-doped carbon materials should consider the ease of fabrication and operational stability of the device.[88,89,92] ITO releases metallic species (*e.g.*, In and Sn) into active materials by diffusion; these quench excitons and trap charge carriers,

Table 3 Summary of flexible PSCs based on conducting polymer electrodes

Substrate	Bottom electrode	Bottom buffer layer	Perovskite	Top buffer layer	Top electrode	Notes
PET	PEDOT:PSS (PH1000)	PEDOT:PSS (AI4083)	$MAPbI_3$	PCBM	Al	PCE 7.6%, declined ∼80% after 2000 bending cycles with r_B = 4 mm. The PCE of the device with the PEDOT:PSS electrode then stabilized whereas that with the metalized indium oxide electrode did not.[28]
PET	PEDOT:PSS (PH1000)	PEI	$MAPbI_3$	Spiro-OMeTAD	Au	PCE 12.4%, no bending test.[50]
PET	PEDOT:PSS (PH1000 with MSA)	PEDOT:PSS (AI4083)	$MAPbI_{3-x}Cl_x$	PCBM/rhodamine/C_{60}/rhodamine/LiF	Ag	PCE 14.7%, declined 27% after 2000 bending cycles with r_B = 2–3 mm.[71]
PET	PEDOT:PSS (PH1000 with DMSO)		$MAPbI_{3-x}Cl_x$	PTCDI/Cr_2O_3/Cr	Au	PCE 12.0%, no bending test.[51]
UV cured shape recovery polymer (NOA 63)	PEDOT:PSS(PH1000)		$MAPbI_{3-x}Cl_x$	PCBM	Ga–In eutectic alloy (EGain)	PCE 10.8%, declined 10% after 1000 bending cycles with r_B = 1 mm. The randomly crumpled device recovered after annealing at 80 °C for 10 s.[83]
PET	PEDOT:PSS(PH1000 with EG)	PEDOT:PSS(AI4083)	$MAPbI_3$	PCBM/TiO_2	Al	PCE 4.9%, declined ∼0% after 100 bending cycles with r_B = 3 mm, whereas the reference device with the PET/ITO anode declined 100%.[72]
PET	Nitric acid annealed PEDOT:PSS based on PH1000	ZnO	Mixed cation perovskite	Spiro-OMeTAD	Nitric acid annealed PEDOT:PSS based on PH1000	PCE 13.9%, declined <10% after 1000 bending cycles with r_B = 5 mm.[8]

Table 4 Summary of PeLEDs based on conducting polymer electrodes

Substrate	Bottom electrode	Bottom buffer layer	Perovskite	Top buffer layer	Top electrode	Notes
Glass	PEDOT:PSS:PFI	—	$MAPbBr_3$:TPBI	TPBI	Al	CE = 42.9 cd A^{-1} (ref. 2)
Glass	PEDOT:PSS:PFI	—	$MAPbBr_3$:TPBI	TPBI	Al	External quantum efficiency = 8.79%[84]
PDMS	PEDOT:PSS:PEO		$MAPbBr_3$:PEO	—	Eutectic indium–gallium	CE = 2.7 cd A^{-1}, luminance = 15 960 cd m^{-2} Sustained after 40% uniaxial strain[75]
Glass	PEDOT:PSS:PFI	—	$FA_{0.9}Cs_{0.1}Br_3$	TPBI	Al	External quantum efficiency = 3.10%[60]
Glass	DMSO/MAI-doped PEDOT:PSS:PFI	—	$MAPbBr_3$:TPBI	TPBI	Al	External quantum efficiency = 10.93%[6]
Glass	PEDOT:PSS:PFI	—	$MAPbBr_3$:TPBI	TPBI	Al	CE = 87.35 cd A^{-1} (ref. 85)
PET	PEDOT:PSS (DMSO + Zonyl®)	—	$MAPbBr_3$	PFN	Ag NW	Maintained 80% of the initial luminance after 400 bending cycles with r_B = 2.5 mm[5]

and consequently degrade the luminescent efficiency in LEDs or photo-voltage in SCs.[31,86,87]

PSC devices must have a low exciton binding energy and long carrier diffusion length of the MHP and the PeLED devices must have a large exciton binding energy and short exciton diffusion length.[2,93] The excitons near carbon materials are easily annihilated, although the carbon electrode does not cause unwanted diffusion of metallic species,[31,87] as an ITO electrode does. Therefore, the interface between the electrode and perovskite active layer should be developed to block excitons and charge carriers. Carbon materials including carbon nanotubes, carbon nanofibers, graphene and graphene oxide have been used in PSCs and PeLEDs as flexible electrodes. The devices have been fabricated in a variety of structures and have a range of properties (Tables 5 and 6).

3.2.1. Carbon nanotubes. Carbon nanotubes (CNTs) have remarkable electrical and mechanical properties that are suitable for use in flexible and stretchable electronic devices. CNTs are several micrometers in length and 2.5–30 nm in diameter.[100] They have been evaluated for various device applications including field emission devices, composites and electrodes.[101–103] A CNT is a carbon allotrope that forms a cylindrical nanostructure that has a very high aspect ratio up to 132 000 000 : 1.[104] CNTs are categorized as single-walled (SWCNTs) and multi-walled (MWCNTs). They are constructed by sp^2 hybridized bonding, which can give unique electrical,

Table 5 Summary of flexible PSCs based on carbon or metal electrodes

Substrate	Bottom electrode	Bottom buffer layer	Perovskite	Top buffer layer	Top electrode	Notes
PET/cross-linkable olefin-type polymer	Graphene	P3HT	$MAPbI_3$	PCBM	Ag	PCE 11.5%, declined 14% after 500 bending cycles with r_B = 1.75 mm.[94]
PEN	Graphene	MoO_3/PEDOT:PSS(AI4083)	$MAPbI_3$	C_{60}/BCP/LiF	Al	PCE 16.8% (avg. 15.0%), declined 10% after 1000 bending cycles with r_B = 2 mm.[95]
PET/APTES	Graphene	$AuCl_3$/PEDOT:PSS	$FAPbI_{3-x}Br_x$	PCBM	Al	PCE 17.9% (avg. 15.6%), declined 25% after 1000 bending cycles with r_B = 4 mm.[96]
PET	Graphene	TiO_2/PCBM	$MAPbI_3$	Spiro-OMeTAD	CSCNTs	PCE 11.9%, declined 14% after 2000 bending cycles with r_B = 4 mm.[34]
PET	Diluted HNO_3–SWNT	PEDOT:PSS	$MAPbI_3$	PCBM	Al	PCE 6.1% (avg. 6.0%), no bending test.[97]
CNT fiber		Compact n-TiO_2/m-TiO_2	$MAPbI_{3-x}Cl_x$	P3HT/SWNT	Ag NW + twisted with another CNT fiber	PCE 3.0%, unlikely to decline after 1000 bending cycles with r_B = 0.3 mm.[98]

Table 6 Summary of PeLEDs based on carbon electrodes

Substrate	Bottom electrode	Bottom buffer layer	Perovskite	Top buffer layer	Top electrode	Notes
Polyacrylate	Single-walled CNTs	—	$MAPbBr_3$:PEO	—	Ag NW	Current efficiency = 0.6 cd A^{-1}, external quantum efficiency = 0.14%[99]
PET	4-Layer graphene (CVD-grown)	PEDOT:PSS:PFI	$MAPbBr_3$:TPBI	TPBI	Al	Current efficiency = 18.0 cd A^{-1}, external quantum efficiency = 3.8% Current density declined 19% after 1200 bending cycles to radius 7.5 mm[87]

physical, and mechanical properties. In contrast, individual CNTs are usually aligned by van der Waals attractive forces between them.

The atomic arrangement of carbon atoms in nanotubes strongly affects their electrical properties. A nanotube that has an armchair structure can be metallic with negligible energy bandgap; in contrast, a nanotube that has a zigzag or chiral structure is semi-conducting with a small energy bandgap.[105] Their unique one-dimensional (1-D) wire-like structure gives a 1-D quantum conduction channel along the tube's axis with ballistic conduction like a quantum resistor.[106] Ballistic conduction is a quantum behavior of electrons in the CNT (SWCNT ropes have $R_S = 10^{-4}\ \Omega\ \text{cm}^{-1}$ at 300 K.[107])

CNTs have been evaluated as electrodes for optoelectronic devices.[108] CNT films for transparent electrodes should have a low R_S and a high optical transmittance T_O, but these parameters are in a trade-off relationship. Minimum industry standards require $R_S < 100\ \Omega\text{sq}^{-1}$ with $T_O > 90\%$ at 550 nm.[109] The ratio of the DC conductivity to the optical conductivity is a commonly used figure of merit for transparent conductors. A transparent electrode requires a high ratio. The relationship between transmittance $T(\lambda)$ at wavelength λ and R_S of thin conducting films can be expressed as

$$T_O(\lambda) = \left(1 + \frac{188.5}{R_s} \times \frac{\sigma_{OP}(\lambda)}{\sigma_{DC}}\right)^{-2},$$

where $\sigma_{OP}(\lambda)$ is the optical conductivity of the film and σ_{DC} is its DC conductivity.[110] To achieve $R_S < 100\ \Omega\text{sq}^{-1}$ and transmittance $>90\%$, σ_{DC}/σ_{OP} should be >35.[109] The optical conductivity of SWNT films is usually $\sim 1.5 \times 10^4$ S m^{-1},[111] so $\sigma_{DC}/\sigma_{OP} > 35$ requires $\sigma_{DC} > 5.3 \times 10^5$ S m^{-1}. Several methods to increase σ_{DC}/σ_{Op} have been reported. Nitric acid treatment increased it to 25.3.[111] Several other studies have developed high σ_{DC}/σ_{Op}.[42,112,113] Although an individual CNT can have σ_{DC} up to 200 000 S cm^{-1},[103] the highest conductivity of randomly-oriented CNT films has been only 6600 S cm^{-1}.[32] The degradation has been attributed to junction resistance between CNTs. Therefore, to increase the conductance of CNTs, their length, width, density, and the film thickness, must be optimized.

CNT films often have high surface roughness, which can impede uniform contact with overlying layers in a device. Non-uniform contact between a photo-active layer and a CNT film electrode can yield many shunt paths, which can cause a low FF and low PCE. The protruding region of the CNT electrode also likely causes leakage current in LEDs due to local shorting effects.[86] A polymer–nanotube composite film can alleviate the bad effects of high surface roughness. Use of PEDOT:PSS with CNTs can decrease the surface roughness of the electrodes and achieve a higher conductivity than CNT-only films.[109,114]

3.2.2. Graphene.

Graphene is a two-dimensional allotrope of carbon in a single-atom-thick honeycomb lattice in an sp^2 hexagonal bonding configuration. Graphene's structure yields peculiar electrical, electronic and optical properties, which could be of benefit for applications in optoelectronic devices. Single-layered graphene usually has T_O ~ 97.7%,[33] so it is suitable for use as a transparent electrode in optoelectronic devices including LEDs and SCs. Also, graphene possesses a high Young's modulus (~1100 GPa) and intrinsic strength (125 GPa).[115] The first transistor made of a single-layer graphene channel fabricated by the scotch tape method exhibited an ambipolar electric field effect with a carrier concentration of 10^{13} cm^{-2} and a very high electron mobility of 10^4 cm^2 $(V\ s)^{-1}$ at room temperature.[116]

Graphene is composed of a single-atom-thick sheet of carbon atoms, so it has high T_O in the whole range of the visible light wavelength. In the visual window, each layer of graphene degrades T_O by 2.3%, independent of the wavelength (450–750 nm).[33] The high T_O of graphene minimizes the absorption of light when incident light passes through a transparent electrode that is composed of a graphene sheet. Therefore, the transmitted light that reaches the photo-active layer, and the number of photo-excited charges, can be maximized.[91,117] Consequently, the photo-active layer can generate a higher current in SCs[91] that use a graphene electrode. The light generated within the EML in LEDs can also be effectively transmitted through a graphene transparent electrode.

A unique carbon bonding structure with sp^2 hybridization of orbitals provides graphene with semi-metallic electrical properties and a zero band-gap. Therefore, electrons in graphene can behave like massless particles with a very high electron mobility (~10^4 cm^2 $(V\ s)^{-1}$).[116] The excellent electrical properties of graphene enable it to efficiently collect charge carriers that are generated in the photo-active layer in SCs,[91] or to efficiently conduct charges into the EML in LEDs.[31,86–89]

Requirements for SCs and LED electrodes include large area, low R_S and ease of patterning of graphene, so the most widely used methods of graphene production for these applications are to use reduced graphene oxide (rGO) grown by chemical synthesis, or graphene grown by CVD. However, rGO has an R_S of at least several kiloohms per square, and even the pristine graphene grown by CVD does not exhibit a sufficiently high conductivity (>200 Ωsq^{-1}).[31] Thus, an additional doping process is necessary before graphene can be used as a transparent electrode in SCs or LEDs.

The electrode WF has a strong influence on the efficiency of a SC or LED. To facilitate efficient collection by the electrode of the charge carriers generated by the photo-active layer, the WF of the electrode must be considered in relation to the energy level of the photo-active layer. The charge injection is also affected by the magnitude of the energy barrier that forms between the electrode and the charge-transport layer (CTL) in LEDs.[31] Graphene usually shows a low WF ~4.4 eV, so the junctions between graphene electrodes and various kinds of charge transport layers or active layers in optoelectronic devices are not suitable for efficient charge collection or injection. Thus, the WF of graphene must be modified to enable efficient device applications.

3.2.3. Surface engineering of carbon electrodes. R_S and the WF of transparent electrodes strongly affect the luminous efficiencies of LEDs and the PCE in SCs. Pristine graphene has a higher R_S (>300 Ωsq^{-1}) and lower WF (~4.4 eV) than those of ITO (~10 Ωsq^{-1}, 4.8 eV); the conventional device architecture of organic or PeLEDs is not suitable to achieve efficient flexible LEDs with graphene anodes. Therefore, in the beginning stages of carbon based anode applications, LEDs that use a pristine graphene anode had very low luminous efficiencies[118,119] because of a large energy barrier to hole injection between the anode and conventional small-molecule organic hole injection layers. However, the luminous efficiencies of flexible OLEDs with graphene anodes were greatly improved by using chemical doping and interface engineering with polymeric hole-injecting buffer layers, because chemical doping and a self-organized gradient hole injection layer composed of a conducting polymer (PEDOT:PSS) and PFI (GraHIL) can compensate for graphene's low conductivity and WF for hole injection (Fig. 13a).[86,90,120] Surface modifications using transition metal oxides (MoO_3,[121] V_2O_5,[122] and WO_3[122]) have been also used to improve the energy-band alignment (Fig. 13b) between graphene and the CTL; these methods reduced R_S compared that of pristine graphene, and yielded high efficiency in OLEDs.

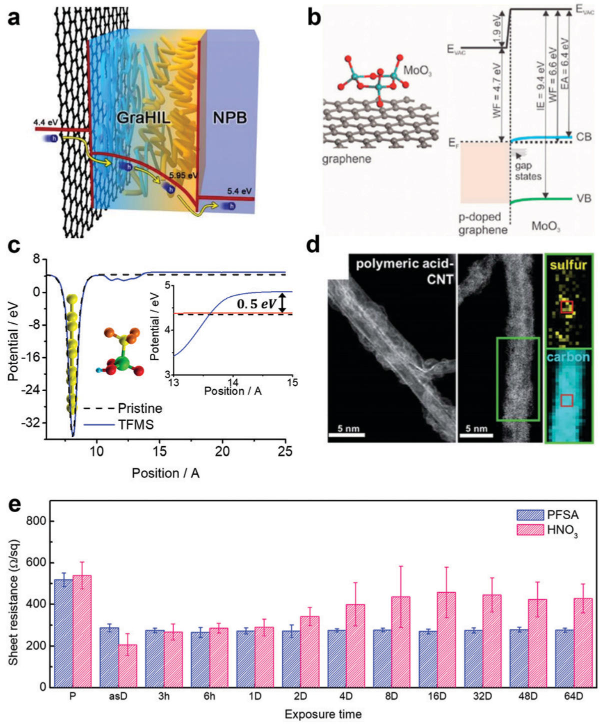

Fig. 13 (a) Schematic diagram of hole injection from graphene to the hole transport layer through the self-organized buffer layer,[86] (Reproduced from ref. 86 with permission from Springer Nature.) (b) energy-band diagram of p-doped graphene/MoO_3,[121] (Reproduced from ref. 121 with permission from John Wiley and Sons.) (c) potential *vs.* position of TFMS on graphene (DFT calculation),[88] (Reproduced from ref. 88 with permission from John Wiley and Sons.) (d) transmission electron microscope image and EELS chemical mapping,[123] (e) R_S *vs.* air-exposure time of PFSA-doped and HNO_3-doped graphene.[89] (Reproduced from ref. 89 with permission from Springer Nature.)

To overcome the disadvantages of pristine carbon nanotubes and graphene for optoelectronic device applications, various doping and interface engineering methods have been explored on carbon-based electrode materials to give tailored electrical and electronic properties. Doping methods for carbon-based electrodes can be mainly classified into (1) substitutional doping, and (2) charge transfer doping that exploits charge transfer on the graphene surface. For the doping of carbon materials for practical optoelectronic devices, several factors should be considered: (1) R_S, (2) WF, (3) air-stability, (4) chemical stability, (5) thermal stability, and (6) film surface smoothness.[31]

Substitutional doping enables control of the physical properties of graphene. Introducing different atoms into CNTs or a graphene lattice modifies its electrical and electronic properties such as the energy band structure (band gap or WF), and electrical properties (R_S) compared to pristine carbon materials.[36,37]

Substitutional doping frequently uses a boron and nitrogen method because the atoms are of similar size to carbon.[37] n-Type-doped carbon nanotubes and graphene have been generally formed by introducing gaseous boronic acid or NH_3 during synthesis of carbon materials.[37,38] The advantage of substitutional doping is that it can precisely control the electrical properties. However, the introduction of different atoms and the subsequently altered electronic structure of low dimensional carbon materials inevitably reduce their electrical conductivity.

Charge-transfer doping of carbon electrode materials is easy, and yields superior electrical doping. Therefore, this method is widely used to tailor the electrical and electronic properties of electrodes for optoelectronic device applications. Charge-transfer processes are usually governed by the relation between the Fermi energy level of carbon materials and energy levels of the dopant material (*i.e.*, highest occupied molecular orbital (HOMO) and lowest unoccupied molecular orbital (LUMO) energy level). When the HOMO energy level of the dopant is higher than the Fermi energy level of the carbon electrode material, or the LUMO level is lower than the Fermi level, charges can transfer between carbon materials and the dopant; this process increases the charge concentration and causes changes in the electrical conductivity and WF of the carbon materials.[31]

p-Type charge-transfer doping of carbon materials has usually used inorganic small molecule acids (*e.g.*, HCl,[39] HNO_3,[86] and H_2SO_4[39]) or metal chlorides (*e.g.*, $AuCl_3$,[86] $IrCl_3$,[40] and $MoCl_3$[40]), which increase the hole concentration, and thereby increase the electrical conductivity and the WF. p-Type graphene electrodes doped with chemicals (HNO_3 and $AuCl_3$) showed greatly reduced R_S ~ 54 and 30 Ωsq^{-1} respectively.[86] Inorganic metal oxides (*e.g.*, MoO_3 and WO_3) have also been used in charge-transfer doping for LED applications of carbon electrodes.[121,122] These methods reduced R_S of CVD-grown few-layer graphene to <50 Ωsq^{-1}, and consequently increased the luminous efficiency of LEDs.

The WF and environmental stability are also important considerations for the charge-transfer doping. The low WF of pristine carbon electrodes, and the large energy barrier between the carbon electrode and charge transport (or injection) layer of LEDs and SCs limit a device's charge injection or collection. However, the WF increase by charge-transfer doping is not high enough to overcome this energy barrier; the usually-used HNO_3 or MoO_3 increase the WF of carbon-based materials by ~0.2 eV.[88,89,121] Even though the metal chloride ($AuCl_3$) dopant has achieved efficient p-type doping and provided high electrical conductivity (~30 Ωsq^{-1}) and a relatively high WF (~5 eV), large metal particles form on the electrode's surface, so they decreased the optical transmittance and introduce protruding short circuit paths in thin-film devices.[86]

Carbon materials that have been doped with small inorganic molecules show an R_S that gradually increases during exposure to air.[86,88,89] To overcome this problem, bis(trifluoromethanesulfonyl) amide (TFSA, $[CF_3SO_2]_2NH$) can be used as an air-stable p-type chemical dopant of CNTs and graphene;[124] the methods reduced R_S by ~70% and the hydrophobic nature of TFSA-doped graphene provided air-stability in ambient conditions for more than two weeks.

Solution-process doping with a small organic acid molecule trifluoromethanesulfonic acid (CF_3SO_3H, TFMS) (Fig. 13c) can maximize the p-type doping effect of graphene and give air-stability to doped graphene.[88] The strong acidity and non-planar configuration of TFMS gave excellent p-type doping effects to graphene (~70% decrease of R_S to ~63 Ωsq^{-1}; ~0.8 eV increase in the surface WF). This simple and strong p-type doping provided high luminous efficiency in OLED devices that used the doped graphene electrodes.

SWCNTs were also doped with TFMS by using a vapor *ex situ* doping method. The process improved the electrical properties and increased the WF, and resulted in higher PCEs in PSCs.[125]

Use of a polymeric acid (perfluorinated sulfonic acid (PFSA), also called perfluorinated ionomer (PFI) as depicted in Fig. 6d) dopant greatly increased the doping stability (>64 d) of p-type doped graphene, and the high ionization potential of PFSA contributed to a large increase in the surface WF of graphene (~1.1 eV).[89] PFSA is completely non-volatile and has a hydrophobic fluorocarbon backbone; these traits made the p-doped graphene extremely stable to air, heat, and chemicals (Fig. 13e). The polymer-doped CNT electrode (Fig. 13d) also showed durability of R_S in ambient conditions for more than 1 y, due to the polymeric acid's strong acidity and chemical stability.[123]

3.2.4. Optoelectronic applications. A four-layer graphene (4LG) anode has been used to fabricate flexible PeLEDs.[87] SLG was grown using CVD on copper foil, and then SLG was stacked using repeated transfer processes to form 4LG. To increase the electrical conductivity of the 4LG anode film, a p-type chemical dopant (HNO_3) was used; it decreased R_S from ~225.7 to ~84.2 Ωsq^{-1}. A conducting polymer interfacial layer that develops a gradient WF (GraHIL)[86,126–128] that increases from graphene to the $MAPbBr_3$ EML was introduced as a surface buffer layer to reduce the energy barrier to hole injection from the 4LG anode. The conventional ITO oxide anode has the critical drawback that metal species diffuse into overlaying layers in LEDs; this process significantly decreases non-radiative recombination in

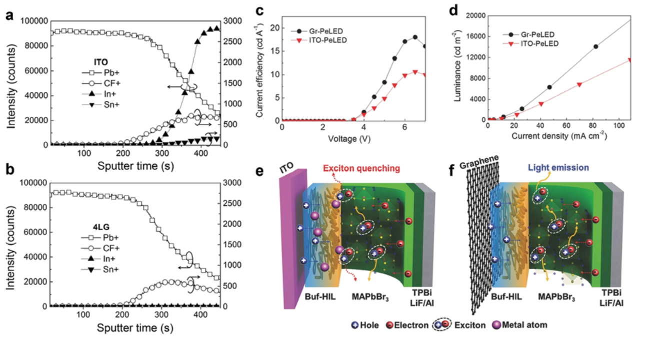

Fig. 14 SIMS depth profiles of Pb^+, CF^+, In^+, and Sn through the polymeric hole injection layer on (a) ITO, and (b) graphene anodes, (c) current efficiency *vs.* voltage and (d) luminance *vs.* current density in $MAPbBr_3$ PeLEDs; and schematic illustration of exciton quenching on (e) ITO, and (f) graphene anodes.[87] (Reproduced from ref. 87 with permission from John Wiley and Sons.)

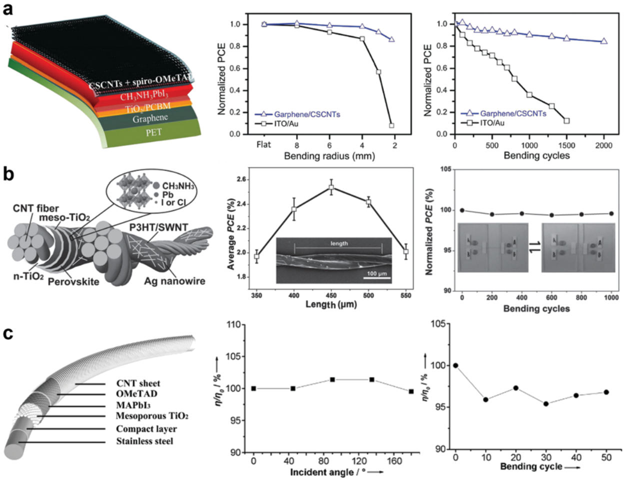

Fig. 15 Schematic architectures and PCE evolution upon bending tests for flexible PSCs with carbon electrodes such as (a) graphene and cross-stacked CNTs,[34] (b) CNT fibers and SWNTs,[98] and (c) CNT sheets.[108] (Reproduced from ref. 34, 98 and 108 with permission from John Wiley and Sons.)

MHP EML because the polycrystalline MHP with large grains has a low exciton binding energy and long exciton diffusion length.[93] Therefore, the chemical instability of an ITO anode degrades the luminous efficiency of PeLEDs. In contrast, graphene is chemically stable and does not cause any diffusion of metallic species, so the flexible PeLEDs fabricated on the 4LG anode enabled higher luminous efficiencies (current efficiency: $\sim$18.0 cd A^{-1} and EQE: $\sim$3.8%) and higher resilience to mechanical bending over 1000 cycles of bending to 1.34% bending strain (Fig. 14).

CNTs and graphene have been used as transparent and solution-processed electrodes in flexible PSCs. Cross-stacked CNT films and graphene electrodes have been used in flexible PSCs that use all-carbon electrodes.[34] Carbon-based flexible PSCs achieved PCE 11.9% with a spiro-OMeTAD HTL, and retained 90% of the original efficiency after 1000 h of light soaking or thermal stress in humid air. They also retained 86% of the original efficiency after 2000 bending cycles with r_B = 4 mm; this result is much superior to PSCs that used ITO, because they delaminated under deformation, while the resistance of conventional flexible electrodes (*i.e.*, ITO/PEN and metal back electrodes) dramatically increased as the number of bending cycles increased (Fig. 15a).

CNTs are also widely used in fiber-shaped and weavable PSCs. A double-twisted PSC that uses CNT fiber electrodes and an easy solution coating process showed a maximum PCE of 3.03%.[98] This PSC based on CNT fibers showed a stable PCE for >96 h in air, and retained its reliability for >1000 bending cycles (Fig. 15b).

A CNT sheet was used in a coaxial fiber-shaped PSC that used a stainless steel fiber with interfacial layers.[129,130] As a transparent top cathode, CNT sheets were wound on top of a fiber PSC that used compact, mesoporous TiO_2 and OMeTAD interfacial layers. The device showed PCE = 3.3% (Fig. 15c).[108]

TiO_2 in fiber PSCs supported by CNT sheets was replaced by synthesizing obelisk-like ZnO arrays; as a result of effective penetration of a second phase into the voids, and rapid charge transport along ZnO axes, +3% of the initial PCE (2.61%) was maintained after bending for 200 cycles.

Section 3.2 has reviewed the electrode properties of carbon materials and their applications in flexible and stretchable perovskite optoelectronics. The appropriate surface modification methods for carbon electrodes yield a low sheet resistance ($\sim$30 Ωsq^{-1})[86,88] and a high WF ($\sim$5.5 eV)[89] with a good optical transparency, but the verification of their mechanical stretchability in practical optoelectronic devices is still incomplete. In theory, graphene has a high mechanical fracture resistance ($\sim$25% facture strain[115]) due to its hexagonal lattice structure with strong bonding between carbons, but practical applications of graphene in stretchable devices have shown limited mechanical fracture strain <5% due to the large number of atomic defects in CVD-grown graphene.[131] Therefore, methods of synthesis and carbon electrode preparation must be improved to yield highly crystalline, defect-free graphene that has practically high mechanical resistance against flexion and stretching. Also, to achieve high-efficiency and stable flexible and stretchable perovskite optoelectronic devices that use carbon electrodes, further research must be conducted about the interface between the carbon electrode and perovskite active materials, to find ways to reduce interface defects and luminance quenching by carbon materials.[93]

3.3. Structured metals (metal fibers/wires/grids) and their composites

This section considers flexible and conductive electrodes based on structured metals (*i.e.* metal foil with nanostructured metal oxides, and metal fibers/wires/grids) and their composite materials for perovskite optoelectronics. Examples include thin metal substrates with nanostructured transparent conducting oxides, metal fibers, metal nanowires, and their composites. Metal or metal composite materials are highly conductive and inexpensive but strategies to overcome their opacity, brittleness, and high fabrication temperature must be developed

Table 7 Summary of flexible PSCs based on structured metals and their composites electrode

Substrate	Bottom electrode	Bottom buffer layer	Perovskite	Top buffer layer	Top electrode	Notes
Ti		Anodized TiO_2 nanotubes	$MAPbI_3$	Spiro-OMeTAD	CNTs	PCE 8.3% (avg. 7.4%), declined 16% after 100 bending cycles with $r_B = 7.5$ mm.[132]
Ti		c-TiO_2/mp-TiO_2	$MAPbI_3$	Spiro-OMeTAD	Ultrathin Ag	PCE 6.2% (avg. 4.1%), declined 1.5% after 100 bending cycles with $r_B = \sim 6$ mm.[133]
Ti		c-TiO_2/mp-Al_2O_3	$MAPbI_{3-x}Cl_x$	Spiro-OMeTAD/ PEDOT:PSS	Ni mesh/PET	PCE 10.3%, declined 7% after 200 bending cycles with $r_B = 50$ mm.[134]
Ti		TiO_2 NW	$MAPbI_3$	PEDOT:PSS	ITO	PCE 13.1% (avg. 10.2%), no bending test.[135]
Ti		c-TiO_2 blocking layer (calcination)	$MAPbI_3$	Spiro-MeOTAD	Ag/ITO	PCE 9.5% (avg. 8.7%), declined 1% after 50 bending cycles with $r_B = 6$ mm.[136]
Ti		c-TiO_2 blocking layer (spray pyrolysis)	$MAPbI_3$	Spiro-OMeTAD	Ag NW spray coating	PCE 7.5%, declined 2.6% after 100 bending cycles with $r_B = 10$ mm.[43]
Ti fiber		TiO_2 (anodization)	$MAPbI_{3-x}Cl_x$	Spiro-MeOTAD	CNT sheet	Average PCE 5.0%, declined 20% after 300 bending cycles with $r_B = 10$ mm, and 10% after 250 stretching cycles with a strain of 30%.[137]
Ti fiber		c-TiO_2/mp-TiO_2	$MAPbI_3$	Spiro-MeOTAD	Ag NWs	PCE 3.9%, declined 7% after 50 bending cycles.[138]
Stainless steel fiber		c-TiO_2/m-TiO_2	$MAPbI_3$	Spiro-OMeTAD	CNT sheet	PCE 3.3%, declined 5% after 50 bending cycles.[129]
Stainless steel fiber		ZnO nanorods	$MAPbI_3$	Spiro-OMeTAD	CNT sheet	PCE 1.0%, declined 7% after 200 bending cycles, and 16% after 100 twisting cycles with an angle of 30°.[130]

Table 8 Summary of PeLEDs based on structured metal and metal composite electrodes

Substrate	Bottom electrode	Bottom buffer layer	Perovskite	Top buffer layer	Top electrode	Notes
Polyacrylate	Single-walled CNTs	—	$MAPbBr_3$:PEO	—	AgNW	Current efficiency = 0.6 cd A^{-1}, external quantum efficiency = 0.14%[99]
AgNW–polymer composite	Ag NWs	PEDOT:PSS	$CH_3NH_3PbBr_3$ nanocrystal	TmPyPB	Al	Current efficiency = 10.4 cd A^{-1}, external quantum efficiency = 2.6% (at 1000 cd m^{-2}) Maintained initial efficiency after 1000 bending cycles with $r_B = 4$ mm[139]
NOA 63/H_2SO_4 treated-PEDOT:PSS/ AgNWcomposite	AgNW	H_2SO_4 treated-PEDOT:PSS	$BA_2FA_2Pb_3Br_{10}$	TPBI	Al	Current efficiency = 17.90 cd A^{-1}, external quantum efficiency = 3.98% Stable operation after 1000 bending cycles with $r_B = 2.5$ mm[140]
Pre-stretched VHB	PI–AgNW composite	PEDOT:PSS	$MAPbBr_3$ nanocrystal	TPBI	Al	Current efficiency = 9.2 cd A^{-1} Maintained luminance after 1000 stretch–release cycles of 20% tensile strain[41]
PET	PEDOT:PSS (DMSO + Zonyl®)	—	$MAPbBr_3$	PFN	Ag NWs	Maintained 80% of initial luminance after 400 bending cycles with $r_B = 2.5$ mm[5]
NOA 63	Ag (80 nm thick)	ZnO/PEI	$CsPbI_3$ nanocrystal	TCTA	MoO_3/Ag/MoO_3	Current efficiency = 0.6 cd A^{-1}, external quantum efficiency = 0.14% Maintained 70% of initial luminance after 1000 bending cycles[141]
SU-8	MoO_3/Au	PEDOT:PSS	$MAPbBr_3$	TPBI	Al	Current efficiency = 3.3 cd A^{-1} Maintained 50% of initial luminance after 1000 bending cycles with $r_B = 5$ mm[142]

before these materials can be used in flexible and stretchable perovskite optoelectronics. The perovskite optoelectronic devices with structured metals or their composite materials have various structures and properties (Tables 7 and 8).

3.3.1. Metal substrates with nanostructured metal oxides and metal fibers. Metal substrates with nanostructured metal oxides or metal fibers can be used simultaneously as an electrode and as a conductive substrate, because they are flexible, and have low R_S, and excellent thermal and mechanical stability, so use of a metal conductive substrate permits development of light-weight, stable, and flexible perovskite optoelectronics.

Metal conductive substrates can withstand heating up to 500 °C, and curing by UV irradiation, so high temperature sintering to form anatase TiO_2 materials as an electron transport layer, and intensive UV curing of TiO_2 paste are possible on the substrate, whereas these processes are not compatible with polymer substrates, However pristine metal foils are inherently rough, so the surface of the conductive metal substrate must be flattened, a patterned insulator layer must be formed to electrically separate the electrodes, and a transparent top electrode must be formed on the photoactive perovskite layer to overcome the opacity of the metal substrate.

To use a metallic conductive substrate in perovskite optoelectronics, Ti foil is firstly electropolished to form a flat surface. Then a patterned insulating SiO_2 layer is deposited on the Ti substrate to form an isolated area that separates the electrodes.[133] As an electron transport layer and hole blocking layer, a TiO_2 film on a Ti substrate can be prepared by calcining the Ti surface at 500 °C,[136] or by a hydrothermal reaction,[135] or by electrochemical oxidation (*i.e.* anodization),[132] or by depositing precursors by spray pyrolysis for compact-TiO_2,[43] or by spin coating for mesoporous-TiO_2.

A titanium dioxide nanowire (TNW) anode on Ti foil provides a light-weight and flexible conductive substrate.[135] A TNW array is synthesized on Ti foil by a facile hydrothermal approach, and then $MAPbI_3$ is used to fill the gaps in the array and provide contact among the TNWs. The resulting TNW anode can provide direct pathways for collection and transport of photo-generated electrons from the perovskite layer.[135]

Highly-ordered TiO_2 nanotube (TNT) arrays can be formed on Ti foil by electrochemical oxidation, also called anodization. TNT arrays can be grown on Ti foil by anodization without deposition of a TiO_2 film, so anodization is scalable and compatible with existing industrial processes.

Anodized TNT arrays can form a deposition scaffold for perovskite loading, or an electron conductor for the perovskite photoactive layer (Fig. 16).[132] A compact TiO_2 (c-TiO_2) layer is deposited on a Ti substrate by spray pyrolysis. A mesoporous TiO_2 (mp-TiO_2) layer is deposited on the c-TiO_2 film by spin-coating and annealed, and then the perovskite is absorbed into the mp-TiO_2 layer. This c-TiO_2/mp-TiO_2 layer on a Ti substrate is used in a way similar to the hole-blocking and electron-transport layer of n–i–p PSCs. An insulating scaffold of Al_2O_3 nanoparticles can also be used on the Ti foil/c-TiO_2 conductive electrode as a perovskite absorber. However, these mesoporous or scaffold materials are not favorable for high stability of flexible perovskites. In a bending test, the PCE of PSCs declined by only 7% after 200 bending cycles, but r_B was 5 cm, which is much larger than the conventional test (r_B = ∼5 mm). The sensitivity to bending may be a result of the brittle nature of the mesoporous TiO_2 or the scaffold absorber in PSCs.[134]

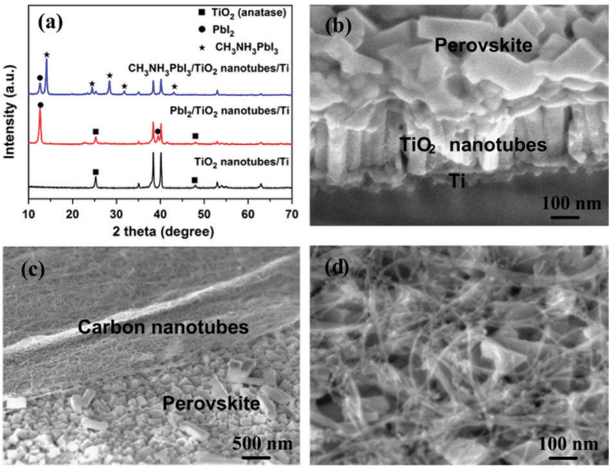

Fig. 16 Highly-ordered anodized TiO_2 nanotube and CNT electrodes for perovskites. (a) XRD patterns, and (b) cross-sectional morphology of the TiO_2 nanotube scaffold with perovskite loading. (c and d) SEM image of the CNT film covering on the perovskite surface.[132] (Reproduced from ref. 132 with permission from Elsevier.)

A Ti fiber with a millimeter-scale diameter has been used as the flexible electrode in fiber PSCs. An elastic-fiber PSC was developed by using an aligned CNT wrapping on an elastic fiber (silicone rubber) as an anode, and a spring-like Ti wire as a cathode. The surface of the spring-like Ti wire is anodized to from TiO_2 nanotubes as an electron-transport layer, and then a perovskite layer and HTM are deposited on the Ti wire/TiO_2 by dip coating. Then an elastic fiber with conductive CNTs is inserted into the spring-like wire Ti/TiO_2/perovskite/spiro-MeOTAD. This novel fiber-shaped perovskite optoelectronic device shows stability under both stretching and bending.

3.3.2. Metal wires/meshes, and their composites. Metal nanowires or metal meshes have outstanding transparency, flexibility, and conductivity, so they can be used as the electrode in perovskite optoelectronics. However, halides (liquid or vapor phase) and halide ions can migrate from the perovskite to the metal nanowire electrodes (*e.g.* Ag and Cu) during fabrication of the perovskite film or operation under electric fields; the strong reaction between the metal and halide degrades the metal nanowires.[143]

Other problems remain to be solved, including WF mismatch and poor surface wettability. The silver nanowire (Ag NW) electrode increases its resistance rapidly after formation of the perovskite film despite the protection on Ag NW by TiO_2 nanocrystals and PEDOT:PSS layers. Therefore, self-assembled graphene oxide (GO) flakes are used on Ag NWs as an anti-corrosive barrier to protect them from degradation by halide compounds (Fig. 17a).[143] The resistance of the pristine Ag NW electrode increases to seven times higher than its initial level before device fabrication, whereas the resistance increase of the Ag NW electrode with the GO protection layer is significantly suppressed, even after 60 min exposure to an ambient atmosphere.

GO flakes have been used as a solder for Ag NW electrodes and as a barrier against oxygen and moisture.[143] To increase the resistance of the anti-corrosive barrier, the coverage of multiple GO flake layers must form a flawless film on the Ag NW surface. To compensate for the poor conductivity of the multiple GO layers in the device, a sodium borohydride ($NaBH_4$) aqueous solution was used in the GO flake solution to improve the conductivity of the GO flakes by a reduction process. However, addition of $NaBH_4$ reduced the WF from −5.12 eV without $NaBH_4$ to −4.65 eV with 80 μmol $NaBH_4$. Moreover, the reduction removes the functional groups on the GO surface, so a GO anti-corrosive barrier is induced to aggregate, and this process degrades the surface wettability for fabrication of a coating layer (*e.g.* PEDOT:PSS). Therefore,

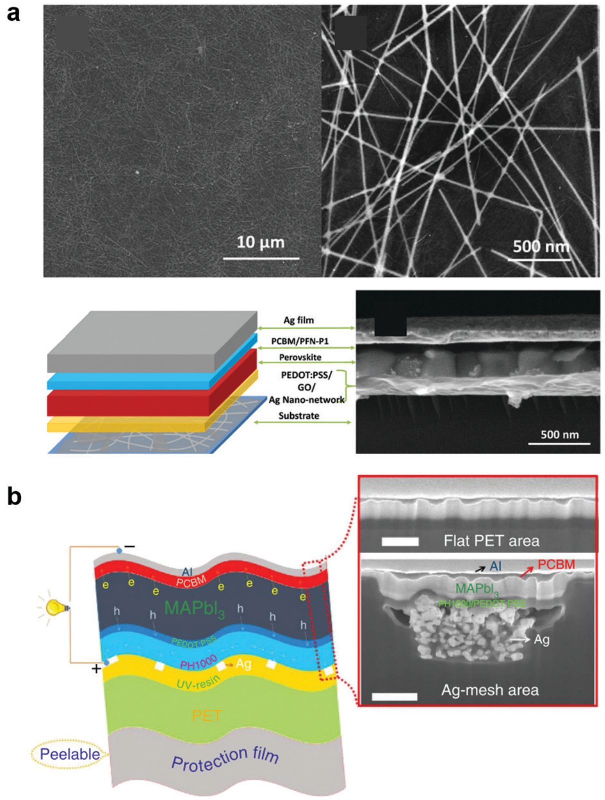

Fig. 17 Device architectures and SEM images of (a) a silver nano-network under the protection of a flawless anti-corrosive GO film,[143] and (b) a silver-mesh embedded in a PET substrate.[35] (Reproduced from ref. 35 with permission from Springer Nature.)

partially-reduced GO is necessary to form an anti-corrosive film with good optical transparency, WF alignment, and surface wetting in the application of perovskite optoelectronics (Fig. 17a).[143]

A hexagonal Ag-mesh embedded in an ultrathin ($\sim$57 µm) ultraviolet-resin-coated PET substrate has been used as a flexible and transparent electrode of perovskite optoelectronics (Fig. 17b).[35] The conductivity of the Ag mesh is 4104 S cm^{-1}, but the coverage of the embedded hexagonal Ag mesh is only 3.2%, so the optical loss is $<$4%. The Ag-mesh embedded PET substrate is laminated on a thick (100 µm) and hardened PET protection film, which is readily peeled off and removed after device fabrication, to fabricate ultrathin flexible perovskite optoelectronics. The embedded Ag mesh is hybridized with a highly-conductive polymer PH1000 ($\sim$0.9 S cm^{-1}), because the effective charge transport length of PH1000 along both the lateral and vertical directions is $<$100 µm, which is larger than half of the diagonal of the Ag mesh honeycomb (90 µm).[35]

A dispersed Ag NW has been used as a transparent top electrode in flexible perovskite optoelectronics fabricated on an opaque bottom substrate.[43] The Ag NW film has $>$80% transmittance in the visible and near-infrared light spectrum (400–1000 nm). The Ag NW electrode is spray-coated on top of the hole transport layer of a perovskite optoelectronic device based on a Ti substrate. The Ag NW solution is dissolved in IPA as a harmless solvent to use with a perovskite and spiro-MeOTAD layer. The PCE of the silver NW devices remained stable over 100 cycles of bending with r_B = $\sim$10 mm.[43]

Ag NW electrodes have also been used in perovskite optoelectronics based on Ti fibers.[138] The energy-level offset between the VBM of spiro-MeOTAD (5.22 eV) and the WF of the as-sprayed Ag NWs (4.5 eV) is decreased by oxygen-plasma treatment of the Ag NWs. However, the PCE of the PSCs with Ag NWs is inferior to PSCs that have conventional metal or TCO electrodes.

3.3.3. Optoelectronic applications.

A TiO$_2$ nanowire (TNW) anode on Ti foil is used in n–i–p PSCs as a light-weight and flexible conductive substrate (Fig. 18a).[135] The as-prepared Ti/TNW anode and PEN/ITO/PEDOT:PSS cathode are assembled using binder clips, and then MAPbI3 in γ-butyrolactone solution is injected into the gap between the two electrodes to sensitize the perovskite photoactive material in TNW arrays in the device (Ti/TNW/perovskite/PEDOT:PSS/ITO/PEN). Under 100 mW cm^{-2} AM 1.5G illumination, PSCs that use the Ti/TNW anode showed PCE = 13.1%, J_{SC} = 21.7 mA cm^{-2}, V_{OC} = 0.94 V, and FF = 0.64. When TiO$_2$ nanoparticles were used on Ti foil, the PCE was lower (9.9%) than when TNWs were used, because the TNW arrays have better electron-transport ability than do TiO$_2$ nanoparticles.[135]

PSCs that use 25 µm Ti foil and anodized TiO$_2$ nanotube arrays achieved a PCE up to 8.31%.[132] The PSC that used Ti/TiO$_2$ nanotubes retained 84% of its initial PCE after 100 cycles of bending with r_B = 7.5 mm. The repeated bending caused micro-sized cracks and delamination at interfaces between different layers of the solar cells, but did not significantly affect the Ti/TiO$_2$ nanotubes (Fig. 18b).[132]

n–i–p PSCs on a conductive electrode of Ti foil have also been developed using the well-known TiO$_2$ deposition process.[136] c-TiO$_2$ and mp-TiO$_2$ layers are used in PSCs constructed on Ti foil (Ti/c-TiO$_2$/mp-TiO$_2$/MAPbI$_3$/spiro-OMeTAD/Ag/ITO) by spray pyrolysis and spin coating (Fig. 18c). An ultrathin Ag layer (1–3 nm) is deposited by thermal evaporation between spiro-MeOTAD and sputtered ITO, to enable use of brittle ITO in the flexible PSCs. The ultrathin Ag layer has several advantages, including low resistivity, high diffusive transmittance, and an ability to provide a crystalline seed layer to orient ITO growth, so a relatively thin (200 nm) and flexible ITO layer can be used in these PSCs. The champion device showed PCE = 11.0%, with J_{SC} = 18.5 mA cm^{-2}, V_{OC} = 0.998 V, and FF = 0.61. In addition, the stability against bending cycles improved as the thickness of the Ag layer was increased. The PCE of the device with a 3 nm-thick Ag layer retained 99% of the initial value after 50 cycles of bending with r_B = 6 mm.

c-TiO$_2$ and Al$_2$O$_3$ nanoparticle layers are also used in PSCs that use Ti foil (Ti/c-TiO$_2$/Al$_2$O$_3$ nanoparticles/MAPbI$_{3-x}$Cl$_x$/spiro-OMeTAD/PEDOT:PSS/transparent-conducting-adhesive/Ni mesh embedded PET) and were deposited by spin coating (Fig. 18d).[134] A flexible and transparent counter-electrode was prepared by deposition of a mixture of pressure-sensitive adhesive and PEDOT:PSS on a PET film that included a Ni mesh. This counter-electrode is laminated onto the surface of

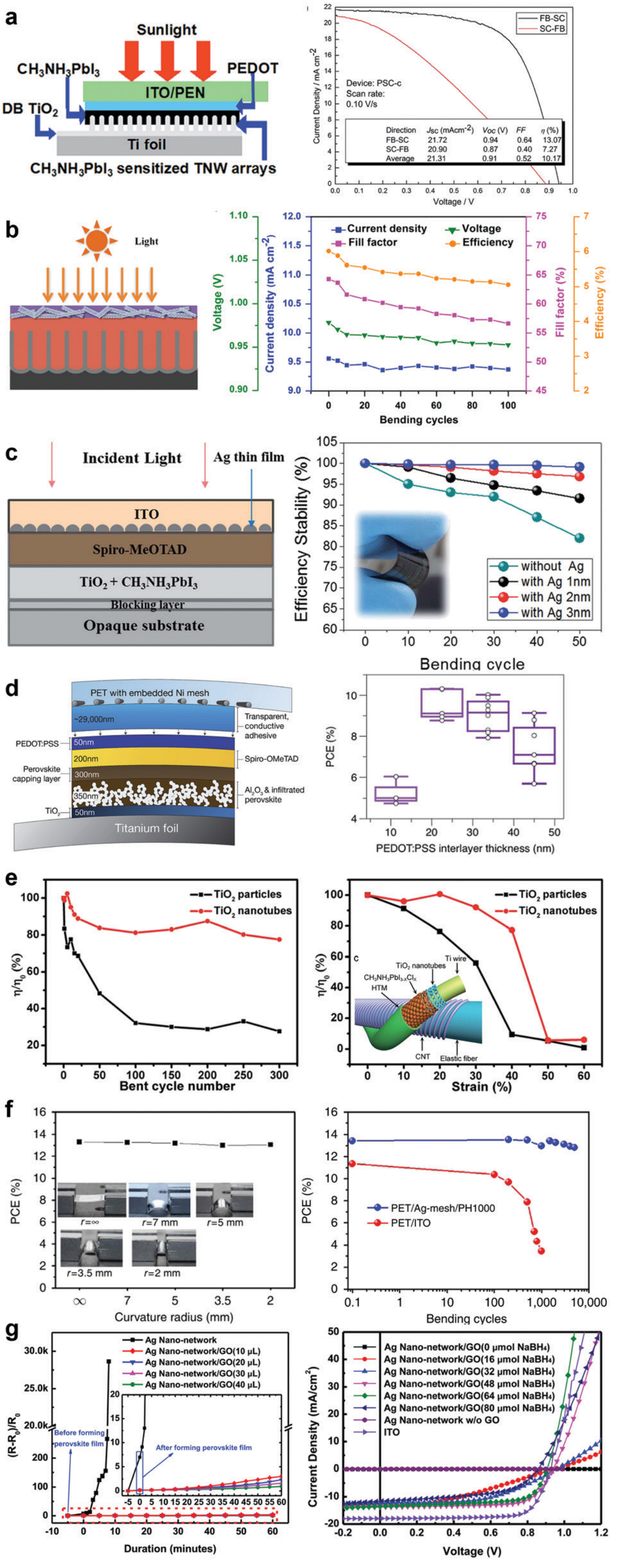

Fig. 18 Conceptual images and device performance of flexible PSCs with (a) TiO_2 nanowires,[135] (b) Ti foil and anodized TiO_2 nanotubes,[132] (Reproduced from ref. 132 with permission from Elsevier.) (c and d) Ti foil,[134,136] (e) aligned CNTs,[137] (f) a Ag-mesh,[35] (Reproduced from ref. 35 with permission from Springer Nature.) and (g) Ag nanowires.[143]

spray-deposited PEDOT:PSS in the bottom device. The transparent conducting adhesive contains only around 1.75% PEDOT:PSS; the rest is dielectric adhesive material, so charge transfer is severely limited. To overcome this limitation, a spray-deposited PEDOT:PSS interfacial layer is used to increase the charge collection and transport from spiro-OMeTAD to the transparent conducting adhesive. The champion device had PCE = 10.3%, with J_{SC} = 17.0 mA cm^{-2}, V_{OC} = 0.98 V, and FF = 0.61. However, the flexibility of the device is limited to a larger r_B = 5 cm than that used in the conventional bending test; this limitation may be a result of the brittle nature of the Al_2O_3 scaffold.[134]

Another flexible and stretchable PSC used a spring-like Ti wire as an anode, and an aligned CNT as a cathode.[137] An elastic fiber with a conductive CNT is inserted into the spring-like Ti wire, so a novel device with the structure of Ti/anodized TiO_2/perovskite/spiro-MeOTAD/CNT/elastic fiber (silicone rubber) was fabricated. The device retained 80% of its original PCE after 300 cycles of bending, and retained 90% of its original PCE after 250 stretching cycles to a strain of 30%. The integration of the material (anodized TiO_2 nanotubes *vs.* pristine TiO_2 nanoparticles), and the geometry (spring-shaped Ti fiber) is effective to lessen stress during stretching and bending (Fig. 18e).

An embedded Ag-mesh electrode in an ultrathin PET substrate can be used as a flexible transparent electrode in a flexible p–i–n PSC (PET/Ag-mesh/PH1000/PEDOT:PSS/perovskite/PCBM/Al) (Fig. 18f). The PH1000 layer and an additional PEDOT:PSS interlayer were deposited on the embedded Ag-mesh to improve charge collection and charge transport from the perovskite photoactive layer. Under 100 mW cm^{-2} AM 1.5G illumination, the champion device had PCE = 14.2%, J_{SC} = 19.5 mA cm^{-2}, V_{OC} = 0.91 V, and FF = 0.80. The PSC with the PET/Ag-mesh electrode also achieved a high ratio of power to device weight (1.96 kW kg^{-1}) due to the ultrathin device. The electrode in this PSC also had high mechanical stability; the device retained 95% of its original PCE after 5000 bending cycles with r_B = 5 mm, whereas that with PET/ITO dropped severely after 100 bending cycles.[35]

Ag NWs and a flawless partially-reduced GO film with a suitable WF and surface wetting properties have been used in p–i–n PSCs (PET/Ag NWs/GO/PEDOT:PSS/peroskite/PCBM/PFN-P1/Ag) (Fig. 18g). Under 100 mW cm^{-2} AM 1.5G illumination, the device constructed on rigid glass showed PCE = 9.23%, J_{SC} = 13.8 mA cm^{-2}, V_{OC} = 0.94 V, and FF = 0.71, whereas the device constructed on PET showed PCE = 7.92%, J_{SC} = 12.7 mA cm^{-2}, V_{OC} = 0.94 V, and FF 0.66.[143]

Fully-printed and flexible PeLEDs were demonstrated using a Ag nanowire cathode and a SWCNT anode.[99] The Ag nanowires were printed on a $MAPbBr_3$–PEO composite EML. The resulting PeLEDs did not show significant luminous degradation under 2% tensile strain, and achieved maximum device efficiencies of 0.6 cd A^{-1} and 0.14%.

A nanowire–polymer composite anode and colloidal $MAPbBr_3$ quantum dots increased the mechanical robustness of PeLEDs.[139] Ag NW networks were introduced into a monomer

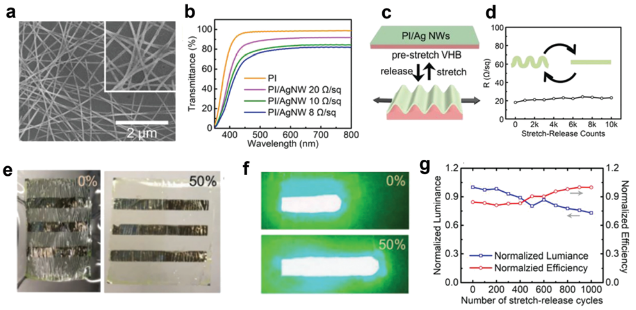

Fig. 19 (a) SEM image of AgNWs, (b) optical transmittance of AgNW films on a polyimide substrate, (c) schematic illustration of the buckling structure of the composite electrode film, (d) change of R_S *vs.* number of stretch–release cycles, (e) optical images of stretchable LEDs fabricated on AgNW electrodes and (f) light emission before and after 50% stretching, and (g) normalized luminance and efficiency of stretchable LEDs *vs.* number of stretch–release cycles.[41] (Reproduced from ref. 41 with permission from John Wiley and Sons.)

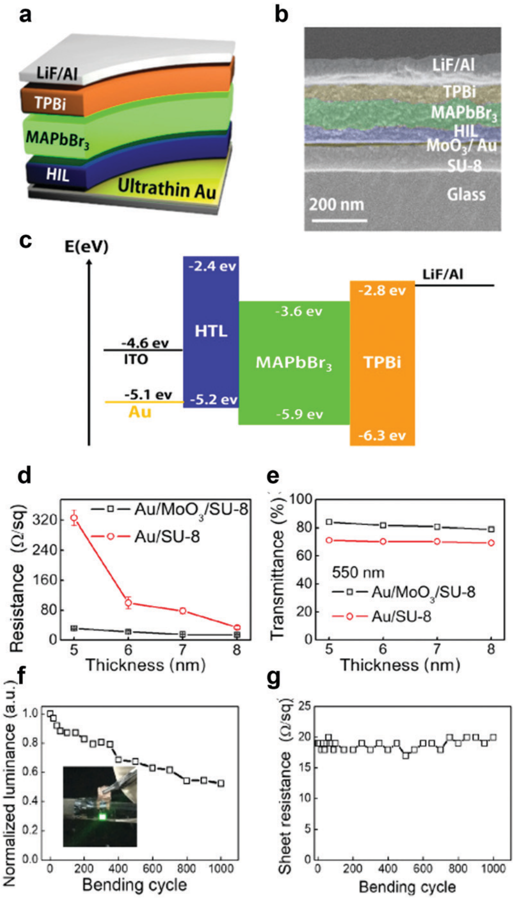

Fig. 20 (a) Device structure, (b) cross-sectional SEM image, and (c) energy band diagram of a $MAPbBr_3$ PeLED on an ultrathin Au electrode, (d) resistance, and (e) transmittance of the Au electrode *versus* MoO_3 thickness between Au and SU-8, and (f) normalized luminance and (g) R_S *vs.* number of bending cycles.[142] (Reprinted with permission from ref. 142 © The Optical Society.)

solution (SR540, SR499, and 2,2-dimethoxy-2-phenylacetophenone), and irradiated with UV to form a free-standing Ag NW composite film as the anode. The flexible perovskite QD LEDs showed mechanical stability against 1000 cycles of bending (r_B = 2.5 mm) as well as improved current, power, and EQE (10.4 cd A^{-1}, 8.1 lm W^{-1}, and 2.6% at 1000 cd m^{-2}).[139]

Ultrathin perovskite QD LEDs (<3 μm) with a surface-wrinkled elastomer substrate were fabricated[41] with a Ag NW network embedded in a 1–2 μm polyimide (PI) film that has a low surface roughness of 0.796 nm as a flexible anode. R_S of the composite electrode was 20 Ωsq^{-1} with 90% optical transmittance at 550 nm (Fig. 19). The buckling structure formation of the composite electrode film increases its stretchability; it maintained its low R_S after 10 000 cycles of stretching with 0–50% strain.[41] A green-emitting perovskite QD LED fabricated on the Ag NW composite anode achieved a current efficiency of 9.2 cd A^{-1}, and operated stably against 1000 stretch–release cycles to 20% tensile strain.[41]

A spray-coating method was used to fabricate a Ag NW cathode on PeLEDs to produce flexible and semitransparent PeLEDs.[5] The Ag NW film showed low $R_S \sim 20.5\ \Omega sq^{-1}$ with 81.3% optical transmittance at 550 nm, and the assembled LEDs showed 48.1% optical transmittance at 550 nm. The Ag NW cathode coated on a conjugated polyelectrolyte (poly[(9,9-bis(3′-(*N*,*N*-dimethylamino)propyl)-2,7-fluorene)-*alt*-2,7-(9,9-dioctylfluornene)], PFN) showed a low increase of R_S with respect to the initial value ($\Delta R/R_0$ = 0.127) after 1000 bending cycles (r_B = 1.0 mm).

Thin metal films have been also used as transparent conducting electrodes in flexible PeLEDs. Flexible $CsPbI_3$ nanocrystal LEDs have been fabricated using an 80 nm-thick Ag film on a photo-polymer flexible substrate as a cathode.[141] The better adhesion of thermally-deposited Ag with the cured photo-polymer (NOA63) than that with the Si substrate enables delamination of the template-stripped cathode composed of Ag/polymer and its ultra-smooth surface morphology (rms roughness ~0.6 nm). A bending test of the fabricated flexible LED to an angle of 180° did not cause cracks or dark spots, and it maintained 70% of its initial luminance after 1000 bending cycles.

Ultrathin Au (7 nm) on a MoO_3/SU-8 modified substrate has been used to fabricate flexible $MAPbBr_3$ LEDs.[142] A MoO_3 seed layer helps to increase nucleation sites and suppress the diffusion of Au atoms for better surface roughness of the ultrathin Au anode (rms roughness: ~0.3 nm). The flexible Au anode showed comparable R_S (~13 Ωsq^{-1}) to that of ITO, and the mechanical flexibility was demonstrated by its unchanged R_S after 1000 bending cycles with r_B = 5 mm (Fig. 20).

Section 3.3 has demonstrated that an electrode composed of metal nanowires or mesh can be a good candidate for use in flexible and stretchable perovskite optoelectronics. Electrodes composed of structured metals and their composites showed poor transparency and resilience in spite of the excellent conductivity (Table 1), so they have usually been considered to be inappropriate for use in flexible and stretchable devices. However, metal nanowire or mesh electrodes (*e.g.*, Ag nanowires or Ag mesh) showed good transparency (Ag nanowires: 90% at 550 nm with 20 Ωsq^{-1},[41] Ag mesh: 96% with 4104 S cm^{-1}),[35] flexibility

(Ag nanowires: stable after 100 cycles of bending with r_B = ~10 mm,[43] stable after 1000 stretch–release cycles to 20% tensile strain,[41] Ag mesh: 95% of its original PCE after 5000 bending cycles with r_B = 5 mm, whereas that with PET/ITO dropped severely after 100 bending cycles[35]), and industrially-viable applicability (Tables 1, 7 and 8). Therefore, metal nanowire or mesh electrodes combined with elastomers or conducting polymers have potential to enable realization of flexible and stretchable perovskite optoelectronics (Tables 7 and 8).

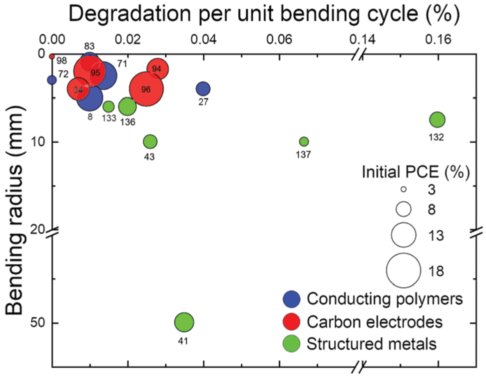

Fig. 21 Summary of flexible PSCs using a flexible electrode of a conducting polymer (blue), carbon electrodes (red), or structured metals (green). Numbers are references. The overall estimations of the normalized efficiency degradation compared with the initial value per unit bending cycle (%) and bending radius (mm), and initial PCE (size of circles) represent the resilient and optoelectronic abilities of the flexible electrodes for PSCs.

4. Conclusion and perspectives

Flexible and stretchable perovskite optoelectronic devices are expected to be used in wearable optoelectronic devices that will supersede conventional rigid display and energy technology. The combination of narrow band emission properties and bandgap tunability of MHPs will provide new opportunity for further applications of optoelectronic devices toward wearable high-color-purity displays and narrow-band LED devices that are required for various bio-medical applications and surveillance.[10] Furthermore, the ultrathin and flexible nature of the perovskite layer for high power-per-weight[35] and shorter energy pay-back time[25] of flexible and stretchable PSCs may enable realization of self-powered wearable smart devices and solar-powered aircraft.

The intrinsic mechanical properties of MHPs and their composition, additive engineering, and polymer composite strategies to increase the mechanical flexibility and stretchability are being investigated. Regarding the mechanical properties of MHPs, engineering of the B-site cation has more influence on the B–X framework's mechanical stiffness than does engineering of the A-site cation. The electronegativity of the halide ion also affects the bonding strength and the mechanical flexibility of B–X inorganic octahedra in MHPs. Also, long and bulky organic halide additives influence on the perovskite active layer's fracture energy against mechanical stress. Perovskite polycrystalline thin films can be further engineered to be suitable for flexible and stretchable optoelectronics, mainly by generating an amorphous perovskite region with many grain boundaries, so perovskite nanocrystals combined with an elastic polymer matrix could be a good option to form intrinsically stretchable perovskite layers. Combined with the superb optoelectronic characteristics of MHPs, their light and soft nature, and further engineering to increase the mechanical stability will widen applications of perovskite materials in next-generation flexible or stretchable optoelectronics.

Flexible and stretchable electrodes must have advanced mechanical (*e.g.*, resilient against bending and stretching, and robust against degradation), optical (*e.g.*, transparent), and electronic (*e.g.*, electric conductivity, and charge transfer at the interface) properties. We have categorized the most-convincing candidates for flexible and stretchable electrode materials (*e.g.*, conducting polymers, low-dimensional carbons, and structured metals) for flexible and stretchable perovskite optoelectronics. To compare them precisely, we obtained a graphical summary of the flexibility parameters regarding PSCs (Fig. 21). Flexible and stretchable electrodes composed of conducting polymers and carbon materials turn out to yield less degradation in bending tests to smaller bending radius, and maintain higher power conversion efficiency than electrodes that are composed of structured metals (*i.e.*, Ti foil, Ti fiber, TiO_2 nanowire, stainless steel fiber). The most reliable PSC with a high bending cycle under a harsh bending environment is the coaxial all-solid-state fiber-shaped PSC that uses CNT fibers (CNT fiber/compact n-TiO_2/m-TiO_2/$MAPbI_{3-x}Cl_x$/P3HT/SWNT/Ag NWs/CNT fibers); however, it has a lower PCE than the others due to processing limitations with a small contact area between the two coiled CNT fiber electrodes. As a consequence, only few candidates of conducting polymers (*i.e.*, PEDOT:PSS with additives), carbon materials (*i.e.*, graphene or CNT films) and silver nanostructures (*i.e.*, Ag fibers/wires/mesh) can achieve the necessary electrical characteristics and flexibility for flexible perovskite optoelectronics. Furthermore, conducting polymers are more easily able to achieve a stretchable electrode with an industry-compatible fabrication process than the others.

PeLEDs that use a flexible electrode composed of conducting polymers and carbon materials also yield higher quantum efficiency and less degradation in bending tests than those of metal electrodes. These characteristics occur because the conducting polymer and carbon electrodes improve not only the flexibility or stretchability but also the optoelectronic characteristics of PeLEDs. Release of metallic species from metal or metal oxide electrodes into the overlying perovskite layers causes quenching of excitons and low efficiency of PeLEDs, and the low resilience of metal electrodes to bending and stretching stress causes limited efficiency of solar cells; however, conducting polymers (*e.g.*, PEDOT:PSS PH1000) and carbon electrodes (*e.g.*, graphene sheets) simultaneously fulfil bending reliability and optoelectronic performance. Compared to the diverse results of PSCs with flexible electrodes that use metal foils and fibers, the devices that use PEDOT:PSS PH1000 or graphene sheets show outstanding and consistent resistance to bending degradation at small bending radius. These conclusions indicate that electrode materials composed of conducting polymers and low-dimensional carbons are the most promising for commercialization of flexible and stretchable PSCs and PeLEDs, because of their mechanical stability and optoelectronic performance.

The up-scaling of flexible/stretchable electrodes and device fabrication techniques is essential for realization of practical device applications. The up-scaling of an electrode film generally increases its sheet resistance and electrical uniformity, thereby increasing the operating voltage and decreasing device efficiencies in large area devices. Furthermore, the large-area thin film fabrications of perovskite active layers likely contain more defects and a loss in film homogeneity;[144] thus, the device performance including the PCE and luminous efficiency is deteriorated in large area devices. Therefore, large area production of electrodes and perovskite active materials should be further developed with compatible roll-to-roll fabrication techniques (*e.g.*, blade coating, inkjet printing, and spray coating) with flexible/stretchable electrode materials.

Environmental stability of devices is one of the challenges in MHPs. Particularly, mechanical strain of flexible/stretchable devices likely form cracks in the active materials, which accelerates perovskite material degradation. Cracks and grain boundaries in polycrystalline thin films can provide an ingression path for molecules such as moisture and oxygen,[145] so high-quality perovskite crystal growth with fewer defects and proper manipulation of grain boundaries are also required for practical operational stability of flexible/stretchable perovskite optoelectronic devices. In addition, a mechanically-robust flexible/stretchable encapsulation technique with a low water-vapor-transmission-rate also has to be developed for flexible and stretchable MHP optoelectronics.

Apart from the MHP active materials and electrodes, the charge transport materials for flexible/stretchable MHP based optoelectronics are particularly required to show more durable electrical and mechanical properties against high strain. Also, the underlying charge transport materials should be further developed to provide a proper template for less-defective perovskite growth, and the interface between the charge transport materials and MHP active materials should be further studied to render minimized interfacial charge carrier traps and non-radiative recombination paths.

Materials for flexible/stretchable substrates are also needed for high-performance PSCs and PeLEDs because the flexibility and stretchability of optoelectronic devices largely depend on their substrate materials. The appropriate substrate (*e.g.*, PET, PI, thermoplastic polyurethane, SEBS, PDMS, stretchable resin, or paper) affects not only the mechanical robustness but also the optoelectronic performances of PSCs and PeLEDs. The desired substrates should have mechanical stability, a smooth surface morphology, high optical transparency, and high-temperature tolerance as well.

Conflicts of interest

There are no conflicts to declare.

Acknowledgements

This work was supported by the National Research Foundation of Korea (NRF) grant funded by the Korea government (MSIT) (NRF-2016R1A3B1908431, 2021R1A2C4002128, 2020R1C1C1008485).

Notes and references

1 K.-G. Lim, S. Ahn, Y.-H. Kim, Y. Qi and T.-W. Lee, *Energy Environ. Sci.*, 2016, **9**, 932–939.

2 H. Cho, S.-H. Jeong, M.-H. Park, Y.-H. Kim, C. Wolf, C.-L. Lee, J. H. Heo, A. Sadhanala, N. S. Myoung, S. Yoo, S. H. Im, R. H. Friend and T.-W. Lee, *Science*, 2015, **350**, 1222–1225.

3 Y.-H. Kim, S. Kim, A. Kakekhani, J. Park, J. Park, Y. H. Lee, H. Xu, S. Nagane, R. B. Wexler, D. H. Kim, S. H. Jo, L. Martínez-Sarti, P. Tan, A. Sadhanala, G. S. Park, Y. W. Kim, B. Hu, H. J. Bolink, S. Yoo, R. H. Friend, A. M. Rappe and T.-W. Lee, *Nat. Photonics*, 2021, **15**, 148.

4 Y.-H. Kim, H. Cho, J. H. Heo, T.-S. Kim, N. S. Myung, C.-L. Lee, S. H. Im and T.-W Lee, *Adv. Mater.*, 2015, **27**(7), 1248–1254.

5 S. Y. Lee, S.-H. Kim, Y. S. Nam, J. C. Yu, S. Lee, D. Bin Kim, E. D. Jung, J.-H. Woo, S. Ahn, S. Lee, K.-J. Choi, J.-Y. Kim and M. H. Song, *Nano Lett.*, 2019, **19**, 971–976.

6 S.-H. Jeong, H. Kim, M.-H. Park, Y. Lee, N. Li, H. K. Seo, T.-H. Han, S. Ahn, J.-M. Heo, K. S. Kim and T.-W. Lee, *Nano Energy*, 2019, **60**, 324–331.

7 D. Alemu, H.-Y. Wei, K.-C. Ho and C.-W. Chu, *Energy Environ. Sci.*, 2012, **5**, 9662.

8 Y. Zhang, Z. Wu, P. Li, L. K. Ono, Y. Qi, J. Zhou, H. Shen, C. Surya and Z. Zheng, *Adv. Energy Mater.*, 2018, **8**, 1701569.

9 J. Feng, *APL Mater.*, 2014, **2**, 81801.

10 Y. Fang, Q. Dong, Y. Shao, Y. Yuan and J. Huang, *Nat. Photonics*, 2015, **9**, 679–686.

11 T.-H. Han, J.-W. Lee, Y. J. Choi, C. Choi, S. Tan, Z. Dai, S.-J. Lee, O. Lin, L. Cai, D. Kim and Y. Yang, *Adv. Mater.*, 2020, **32**, 1905674.

12 Y. Rakita, S. R. Cohen, N. K. Kedem, G. Hodes and D. Cahen, *MRS Commun.*, 2015, **5**, 623–629.

13 S. Sun, F. H. Isikgor, Z. Deng, F. Wei, G. Kieslich, P. D. Bristowe, J. Ouyang and A. K. Cheetham, *ChemSusChem*, 2017, **10**, 3740–3745.

14 S. Sun, Y. Fang, G. Kieslich, T. J. White and A. K. Cheetham, *J. Mater. Chem. A*, 2015, **3**, 18450–18455.

15 J. Yu, M. Wang and S. Lin, *ACS Nano*, 2016, **10**, 11044–11057.

16 M. A. Reyes-Martinez, A. L. Abdelhady, M. I. Saidaminov, D. Y. Chung, O. M. Bakr, M. G. Kanatzidis, W. O. Soboyejo and Y.-L. Loo, *Adv. Mater.*, 2017, **29**, 1606556.

17 L. Zhao, N. Rolston, K. M. Lee, X. Zhao, M. A. Reyes-Martinez, N. L. Tran, Y.-W. Yeh, N. Yao, G. D. Scholes, Y.-L. Loo, A. Selloni, R. H. Dauskardt and B. P. Rand, *Adv. Funct. Mater.*, 2018, **28**, 1802060.

18 H. Zhou, J. Park, Y. Lee, J.-M. Park, J.-H. Kim, J. S. Kim, H.-D. Lee, S. H. Jo, X. Cai, L. Li, X. Sheng, H. J. Yun, J.-W. Park, J.-Y. Sun and T.-W. Lee, *Adv. Mater.*, 2020, DOI: 10.1002/adma.202001989.

19 N. Rolston, B. L. Watson, C. D. Bailie, M. D. McGehee, J. P. Bastos, R. Gehlhaar, J.-E. Kim, D. Vak, A. T. Mallajosyula, G. Gupta, A. D. Mohite and R. H. Dauskardt, *Extreme Mech. Lett.*, 2016, **9**, 353–358.

20 F. Wei, Z. Deng, S. Sun, F. Zhang, D. M. Evans, G. Kieslich, S. Tominaka, M. A. Carpenter, J. Zhang, P. D. Bristowe and A. K. Cheetham, *Chem. Mater.*, 2017, **29**, 1089–1094.

21 Q. Tu, I. Spanopoulos, S. Hao, C. Wolverton, M. G. Kanatzidis, G. S. Shekhawat and V. P. Dravid, *ACS Appl. Mater. Interfaces*, 2018, **10**, 22167–22173.

22 Y. Wang, J. He, H. Chen, J. Chen, R. Zhu, P. Ma, A. Towers, Y. Lin, A. J. Gesquiere, S.-T. Wu and Y. Dong, *Adv. Mater.*, 2016, **28**, 10710–10717.

23 C. C. Lin, D.-H. Jiang, C.-C. Kuo, C.-J. Cho, Y.-H. Tsai, T. Satoh and C. Su, *ACS Appl. Mater. Interfaces*, 2018, **10**, 2210–2215.

24 E. Ercan, P.-C. Tsai, J.-Y. Chen, J.-Y. Lam, L.-C. Hsu, C.-C. Chueh and W.-C. Chen, *ACS Appl. Mater. Interfaces*, 2019, **11**, 23605–23615.

25 K.-G. Lim, S. G. Ji, J. Y. Kim and T.-W. Lee, *Small Methods*, 2020, **4**, 1–28.

26 X. Fan, J. Wang, H. Wang, X. Liu and H. Wang, *ACS Appl. Mater. Interfaces*, 2015, **7**, 16287–16295.

27 M. Vosgueritchian, D. J. Lipomi and Z. Bao, *Adv. Funct. Mater.*, 2012, **22**, 421–428.

28 K. Poorkazem, D. Liu and T. L. Kelly, *J. Mater. Chem. A*, 2015, **3**, 9241–9248.

29 H. M. Kim, Y. C. Kim, H. J. An and J.-M. Myoung, *J. Alloys Compd.*, 2020, **819**, 153360.

30 M. Y. Teo, N. Kim, S. Kee, B. S. Kim, G. Kim, S. Hong, S. Jung and K. Lee, *ACS Appl. Mater. Interfaces*, 2017, **9**, 819–826.

31 T.-H. Han, H. Kim, S.-J. Kwon and T.-W. Lee, *Mater. Sci. Eng., R*, 2017, **118**, 1–43.

32 D. S. Hecht, L. Hu and G. Irvin, *Adv. Mater.*, 2011, **23**, 1482–1513.

33 R. R. Nair, P. Blake, A. N. Grigorenko, K. S. Novoselov, T. J. Booth, T. Stauber, N. M. R. Peres and A. K. Geim, *Science*, 2008, **320**, 1308.

34 Q. Luo, H. Ma, Q. Hou, Y. Li, J. Ren, X. Dai, Z. Yao, Y. Zhou, L. Xiang, H. Du, H. He, N. Wang, K. Jiang, H. Lin, H. Zhang and Z. Guo, *Adv. Funct. Mater.*, 2018, **28**, 1706777.

35 Y. Y. Li, L. Meng, Y. (Michael) Yang, G. Xu, Z. Hong, Q. Chen, J. You, G. Li, Y. (Michael) Yang and Y. Y. Li, *Nat. Commun.*, 2016, **7**, 10214.

36 P. A. Denis, *Chem. Phys. Lett.*, 2010, **492**, 251–257.

37 L. S. Panchakarla, K. S. Subrahmanyam, S. K. Saha, A. Govindaraj, H. R. Krishnamurthy, U. V. Waghmare and C. N. R. Rao, *Adv. Mater.*, 2009, **21**, 4726–4730.

38 D. Wei, Y. Liu, Y. Wang, H. Zhang, L. Huang and G. Yu, *Nano Lett.*, 2009, **9**, 1752–1758.

39 S. Bae, H. Kim, Y. Lee, X. Xu, J.-S. Park, Y. Zheng, J. Balakrishnan, T. Lei, H. Ri Kim, Y. Il Song, Y.-J. Kim, K. S. Kim, B. Ozyilmaz, J.-H. Ahn, B. H. Hong and S. Iijima, *Nat. Nanotechnol.*, 2010, **5**, 574–578.

40 K. C. Kwon, K. S. Choi and S. Y. Kim, *Adv. Funct. Mater.*, 2012, **22**, 4724–4731.

41 Y.-F. Li, S.-Y. Chou, P. Huang, C. Xiao, X. Liu, Y. Xie, F. Zhao, Y. Huang, J. Feng, H. Zhong, H.-B. Sun and Q. Pei, *Adv. Mater.*, 2019, **31**, 1807516.

42 L. Hu, D. S. Hecht and G. Grüner, *Nano Lett.*, 2004, **4**, 2513–2517.

43 M. Lee, Y. Ko, B. K. Min and Y. Jun, *ChemSusChem*, 2016, **9**, 31–35.

44 P. Li, K. Sun and J. Ouyang, *ACS Appl. Mater. Interfaces*, 2015, **7**, 18415–18423.

45 Y. Wang, C. Zhu, R. Pfattner, H. Yan, L. Jin, S. Chen, F. Molina-Lopez, F. Lissel, J. Liu, N. I. Rabiah, Z. Chen, J. W. Chung, C. Linder, M. F. Toney, B. Murmann and Z. Bao, *Sci. Adv.*, 2017, **3**, 1–11.

46 C. Badre, L. Marquant, A. M. Alsayed and L. A. Hough, *Adv. Funct. Mater.*, 2007, **22**, 2723–2727.

47 S. Kee, N. Kim, B. Park, B. S. Kim, S. Hong, J. H. Lee, S. Jeong, A. Kim, S. Y. Jang and K. Lee, *Adv. Mater.*, 2018, **30**, 1–7.

48 T. S. Hansen, K. West, O. Hassager and N. B. Larsen, *Adv. Funct. Mater.*, 2007, **17**, 3069–3073.

49 C. Teng, X. Lu, Y. Zhu, M. Wan and L. Jiang, *RSC Adv.*, 2013, **3**, 7219–7223.

50 L. Chen, X. Xie, Z. Liu and E. C. Lee, *J. Mater. Chem. A*, 2017, **5**, 6974–6980.

51 M. Kaltenbrunner, G. Adam, E. D. Głowacki, M. Drack, R. Schwödiauer, L. Leonat, D. H. Apaydin, H. Groiss, M. C. Scharber, M. S. White, N. S. Sariciftci and S. Bauer, *Nat. Mater.*, 2015, **14**, 1032–1039.

52 A. W. M. Diah, J. P. Quirino, W. Belcher and C. I. Holdsworth, *Electrophoresis*, 2014, **35**, 1976–1983.

53 I. Lee, G. W. Kim, M. Yang and T. S. Kim, *ACS Appl. Mater. Interfaces*, 2016, **8**, 302–310.

54 J. Ouyang, C. W. Chu, F. C. Chen, Q. Xu and Y. Yang, *Adv. Funct. Mater.*, 2005, **15**, 203–208.

55 Y. H. Kim, C. Sachse, M. L. MacHala, C. May, L. Müller-Meskamp and K. Leo, *Adv. Funct. Mater.*, 2011, **21**, 1076–1081.

56 N. Kim, S. Kee, S. H. Lee, B. H. Lee, Y. H. Kahng, Y. R. Jo, B. J. Kim and K. Lee, *Adv. Mater.*, 2014, **26**, 2268–2272.

57 M. Döbbelin, R. Marcilla, M. Salsamendi, C. Pozo-Gonzalo, P. M. Carrasco, J. A. Pomposo and D. Mecerreyes, *Chem. Mater.*, 2007, **19**, 2147–2149.

58 S. I. Na, G. Wang, S. S. Kim, T. W. Kim, S. H. Oh, B. K. Yu, T. Lee and D. Y. Kim, *J. Mater. Chem.*, 2009, **19**, 9045–9053.

59 T.-W. Lee and Y. Chung, *Adv. Funct. Mater.*, 2008, **18**, 2246–2252.

60 H. Cho, J. S. Kim, C. Wolf, Y.-H. Kim, H. J. Yun, S.-H. Jeong, A. Sadhanala, V. Venugopalan, J. W. Choi, C. L. Lee, R. H. Friend and T.-W. Lee, *ACS Nano*, 2018, **12**, 2883–2892.

61 T.-W. Lee, Y. Chung, O. Kwon and J.-J. Park, *Adv. Funct. Mater.*, 2007, **17**, 390–396.

62 K.-G. Lim, H. Kim, J. Jeong, H. Kim, J. Y. Kim and T.-W. Lee, *Adv. Mater.*, 2014, **26**, 6461.

63 J. Ciro, S. Mesa, J. I. Uribe, M. A. Mejía-Escobar, D. Ramirez, J. F. Montoya, R. Betancur, H. S. Yoo, N. G. Park and F. Jaramillo, *Nanoscale*, 2017, **9**, 9440–9446.

64 Y. Li, Y. Zhao, Q. Chen, Y. Yang, Y. Liu, Z. Hong, Z. Liu, Y. T. Hsieh, L. Meng, Y. Li and Y. Yang, *J. Am. Chem. Soc.*, 2015, **137**, 15540–15547.

65 Z. Wang, D. P. McMeekin, N. Sakai, S. van Reenen, K. Wojciechowski, J. B. Patel, M. B. Johnston and H. J. Snaith, *Adv. Mater.*, 2017, **29**(5), 1604186.

66 N. J. Jeon, H. Na, E. H. Jung, T. Y. Yang, Y. G. Lee, G. Kim, H. W. Shin, S. Il Seok, J. Lee and J. Seo, *Nat. Energy*, 2018, **3**, 682–689.

67 J. H. Yun, I. Lee, T. S. Kim, M. J. Ko, J. Y. Kim and H. J. Son, *J. Mater. Chem. A*, 2015, **3**, 22176–22182.

68 Y. C. Kim, T. Y. Yang, N. J. Jeon, J. Im, S. Jang, T. J. Shin, H. W. Shin, S. Kim, E. Lee, S. Kim, J. H. Noh, S. I. Seok and J. Seo, *Energy Environ. Sci.*, 2017, **10**, 2109–2116.

69 J. A. Christians, P. Schulz, J. S. Tinkham, T. H. Schloemer, S. P. Harvey, B. J. Tremolet De Villers, A. Sellinger, J. J. Berry and J. M. Luther, *Nat. Energy*, 2018, **3**, 68–74.

70 Y.-K. Wang, Z.-C. Yuan, G.-Z. Shi, Y.-X. Li, Q. Li, F. Hui, B.-Q. Sun, Z.-Q. Jiang and L.-S. Liao, *Adv. Funct. Mater.*, 2016, **26**, 1375–1381.

71 K. Sun, P. Li, Y. Xia, J. Chang and J. Ouyang, *ACS Appl. Mater. Interfaces*, 2015, **7**, 15314–15320.

72 M. Dianetti, F. Di Giacomo, G. Polino, C. Ciceroni, A. Liscio, A. D'Epifanio, S. Licoccia, T. M. Brown, A. Di Carlo and F. Brunetti, *Sol. Energy Mater. Sol. Cells*, 2015, **140**, 150–157.

73 S.-H. Jeong, S.-H. Woo, T.-H. Han, M.-H. Park, H. Cho, Y.-H. Kim, H. Cho, H. Kim, S. Yoo and T.-W. Lee, *NPG Asia Mater.*, 2017, **9**, e411.

74 S. Ahn, M.-H. Park, S.-H. Jeong, Y.-H. Kim, J. Park, S. Kim, H. Kim, H. Cho, C. Wolf, M. Pei, H. Yang and T.-W. Lee, *Adv. Funct. Mater.*, 2019, **29**, 1807535.

75 S. G. R. Bade, X. Shan, P. T. Hoang, J. Li, T. Geske, L. Cai, Q. Pei, C. Wang and Z. Yu, *Adv. Mater.*, 2017, **29**, 1607053.

76 K. Lim, S. Jung, S. Lee, J. Heo, J. Park, J. W. Kang, Y. C. Kang and D. G. Kim, *Org. Electron.*, 2014, **15**, 1849–1855.

77 B. Vaagensmith, K. M. Reza, M. D. N. Hasan, H. Elbohy, N. Adhikari, A. Dubey, N. Kantack, E. Gaml and Q. Qiao, *ACS Appl. Mater. Interfaces*, 2017, **9**, 35861–35870.

78 C. Yeon, S. J. Yun, J. Kim and J. W. Lim, *Adv. Electron. Mater.*, 2015, **1**, 1500121.

79 J. Ouyang, *ACS Appl. Mater. Interfaces*, 2013, **5**, 13082–13088.

80 J. H. Lee, Y. R. Jeong, G. Lee, S. W. Jin, Y. H. Lee, S. Y. Hong, H. Park, J. W. Kim, S. S. Lee and J. S. Ha, *ACS Appl. Mater. Interfaces*, 2018, **10**, 28027–28035.

81 X. Fan, N. Wang, J. Wang, B. Xu and F. Yan, *Mater. Chem. Front.*, 2018, **2**, 355–361.

82 C. Yeon, G. Kim, J. W. Lim and S. J. Yun, *RSC Adv.*, 2017, **7**, 5888–5897.

83 M. Park, H. J. Kim, I. Jeong, J. Lee, H. Lee, H. J. Son, D.-E. Kim and M. J. Ko, *Adv. Energy Mater.*, 2015, **5**, 1501406.

84 M.-H. Park, S.-H. Jeong, H.-K. Seo, C. Wolf, Y.-H. Kim, H. Kim, J. Byun, J. S. Kim, H. Cho and T.-W. Lee, *Nano Energy*, 2017, **42**, 157–165.

85 M.-H. Park, J. Park, J. Lee, H. S. So, H. Kim, S.-H. Jeong, T.-H. Han, C. Wolf, H. Lee, S. Yoo and T.-W. Lee, *Adv. Funct. Mater.*, 2019, **29**, 1902017.

86 T.-H. Han, Y. Lee, M.-R. Choi, S.-H. Woo, S.-H. Bae, B. H. Hong, J.-H. Ahn and T.-W. Lee, *Nat. Photonics*, 2012, **6**, 105–110.

87 H.-K. Seo, H. Kim, J. Lee, M.-H. Park, S.-H. Jeong, Y.-H. Kim, S.-J. Kwon, T.-H. Han, S. Yoo and T.-W. Lee, *Adv. Mater.*, 2017, **29**, 1605587.

88 T.-H. Han, S.-J. Kwon, N. Li, H.-K. Seo, W. Xu, K. S. Kim and T.-W. Lee, *Angew. Chem., Int. Ed.*, 2016, **55**, 6197–6201.

89 S.-J. Kwon, T.-H. Han, T. Y. Ko, N. Li, Y. Kim, D. J. Kim, S.-H. Bae, Y. Yang, B. H. Hong, K. S. Kim, S. Ryu and T.-W. Lee, *Nat. Commun.*, 2018, **9**, 2037.

90 T.-H. Han, M.-H. Park, S.-J. Kwon, S.-H. Bae, H.-K. Seo, H. Cho, J.-H. Ahn and T.-W. Lee, *NPG Asia Mater.*, 2016, **8**, e303.

91 H. Kim, S.-H. Bae, T.-H. Han, K.-G. Lim, J.-H. Ahn and T.-W. Lee, *Nanotechnology*, 2013, **25**, 14012.

92 S.-J. Kwon, T.-H. Han, Y.-H. Kim, T. Ahmed, H.-K. Seo, H. Kim, D. J. Kim, W. Xu, B. H. Hong, J.-X. Zhu and T.-W. Lee, *ACS Appl. Mater. Interfaces*, 2018, **10**, 4874–4881.

93 S. D. Stranks, G. E. Eperon, G. Grancini, C. Menelaou, M. J. P. Alcocer, T. Leijtens, L. M. Herz, A. Petrozza and H. J. Snaith, *Science*, 2013, **342**, 341–344.

94 Z. Liu, P. You, C. Xie, G. Tang and F. Yan, *Nano Energy*, 2016, **28**, 151–157.

95 J. Yoon, H. Sung, G. Lee, W. Cho, N. Ahn, H. S. Jung and M. Choi, *Energy Environ. Sci.*, 2017, **10**, 337–345.

96 J. H. Heo, D. H. Shin, M. H. Jang, M. L. Lee, M. G. Kang and S. H. Im, *J. Mater. Chem. A*, 2017, **5**, 21146–21152.

97 I. Jeon, T. Chiba, C. Delacou, Y. Guo, A. Kaskela, O. Reynaud, E. I. Kauppinen, S. Maruyama and Y. Matsuo, *Nano Lett.*, 2015, **15**, 6665–6671.

98 R. Li, X. Xiang, X. Tong, J. Zou and Q. Li, *Adv. Mater.*, 2015, **27**, 3831–3835.

99 S. G. R. Bade, J. Li, X. Shan, Y. Ling, Y. Tian, T. Dilbeck, T. Besara, T. Geske, H. Gao, B. Ma, K. Hanson, T. Siegrist, C. Xu and Z. Yu, *ACS Nano*, 2016, **10**, 1795–1801.

100 S. Iijima and T. Ichihashi, *Nature*, 1993, **363**, 603–605.

101 J. W. G. Wilder, L. C. Venema, A. G. Rinzler, R. E. Smalley and C. Dekker, *Nature*, 1998, **391**, 59–62.

102 T. W. Odom, J.-L. Huang, P. Kim and C. M. Lieber, *Nature*, 1998, **391**, 62–64.

103 T. W. Ebbesen, H. J. Lezec, H. Hiura, J. W. Bennett, H. F. Ghaemi and T. Thio, *Nature*, 1996, **382**, 54–56.

104 X. Wang, Q. Li, J. Xie, Z. Jin, J. Wang, Y. Li, K. Jiang and S. Fan, *Nano Lett.*, 2009, **9**, 3137–3141.

105 X. Lu and Z. Chen, *Chem. Rev.*, 2005, **105**, 3643–3696.

106 S. Frank, P. Poncharal, Z. L. Wang and W. A. de Heer, *Science*, 1998, **280**, 1744–1746.

107 A. Thess, R. Lee, P. Nikolaev, H. Dai, P. Petit, J. Robert, C. Xu, Y. H. Lee, S. G. Kim, A. G. Rinzler, D. T. Colbert, G. E. Scuseria, D. Tománek, J. E. Fischer and R. E. Smalley, *Science*, 1996, **273**, 483–487.

108 Z. Wu, Z. Chen, X. Du, J. M. Logan, J. Sippel, M. Nikolou, K. Kamaras, J. R. Reynolds, D. B. Tanner, A. F. Hebard and A. G. Rinzler, *Science*, 2004, **305**, 1273–1276.

109 S. De, P. E. Lyons, S. Sorel, E. M. Doherty, P. J. King, W. J. Blau, P. N. Nirmalraj, J. J. Boland, V. Scardaci, J. Joimel and J. N. Coleman, *ACS Nano*, 2009, **3**, 714–720.

110 M. Dressel and G. Grüner, *Electrodynamics of Solids: Optical Properties of Electrons in Matter*, 2002.

111 H.-Z. Geng, D. S. Lee, K. K. Kim, G. H. Han, H. K. Park and Y. H. Lee, *Chem. Phys. Lett.*, 2008, **455**, 275–278.

112 C. Park, Z. Ounaies, K. A. Watson, R. E. Crooks, J. Smith, S. E. Lowther, J. W. Connell, E. J. Siochi, J. S. Harrison and T. L. S. Clair, *Chem. Phys. Lett.*, 2002, **364**, 303–308.

113 D. Hecht, L. Hu and G. Grüner, *Appl. Phys. Lett.*, 2006, **89**, 133112.

114 F. M. Blighe, Y. R. Hernandez, W. J. Blau and J. N. Coleman, *Adv. Mater.*, 2007, **19**, 4443–4447.

115 C. Lee, X. D. Wei, J. W. Kysar and J. Hone, *Science*, 2008, **321**, 385.

116 K. S. Novoselov, A. K. Geim, S. V. Morozov, D. Jiang, Y. Zhang, S. V. Dubonos, I. V. Grigorieva and A. A. Firsov, *Science*, 2004, **306**, 666–669.

117 H. Kim, J. Byun, S.-H. Bae, T. Ahmed, J.-X. Zhu, S.-J. Kwon, Y. Lee, S.-Y. Min, C. Wolf, H.-K. Seo, J.-H. Ahn and T.-W. Lee, *Adv. Energy Mater.*, 2016, **6**, 1600172.

118 J. Wu, M. Agrawal, H. A. Becerril, Z. Bao, Z. Liu, Y. Chen and P. Peumans, *ACS Nano*, 2010, **4**, 43–48.

119 T. Sun, Z. L. Wang, Z. J. Shi, G. Z. Ran, W. J. Xu, Z. Y. Wang, Y. Z. Li, L. Dai and G. G. Qin, *Appl. Phys. Lett.*, 2010, **96**, 133301.

120 J. Lee, T.-H. Han, M.-H. Park, D. Y. Jung, J. Seo, H.-K. Seo, H. Cho, E. Kim, J. Chung, S.-Y. Choi, T.-S. Kim, T.-W. Lee and S. Yoo, *Nat. Commun.*, 2016, **7**, 11791.

121 J. Meyer, P. R. Kidambi, B. C. Bayer, C. Weijtens, A. Kuhn, A. Centeno, A. Pesquera, A. Zurutuza, J. Robertson and S. Hofmann, *Sci. Rep.*, 2014, **4**, 5380.

122 A. Kuruvila, P. R. Kidambi, J. Kling, J. B. Wagner, J. Robertson, S. Hofmann and J. Meyer, *J. Mater. Chem. C*, 2014, **2**, 6940–6945.

123 I. Jeon, C. Delacou, H. Okada, G. E. Morse, T.-H. Han, Y. Sato, A. Anisimov, K. Suenaga, E. I. Kauppinen, S. Maruyama and Y. Matsuo, *J. Mater. Chem. A*, 2018, **6**, 14553–14559.

124 S. Tongay, K. Berke, M. Lemaitre, Z. Nasrollahi, D. B. Tanner, A. F. Hebard and B. R. Appleton, *Nanotechnology*, 2011, **22**, 425701.

125 J.-W. Lee, I. Jeon, H.-S. Lin, S. Seo, T.-H. Han, A. Anisimov, E. I. Kauppinen, Y. Matsuo, S. Maruyama and Y. Yang, *Nano Lett.*, 2019, **19**, 2223–2230.

126 T.-H. Han, M.-R. Choi, S.-H. Woo, S.-Y. Min, C.-L. Lee and T.-W. Lee, *Adv. Mater.*, 2012, **24**, 1487–1493.

127 T.-H. Han, W. Song and T.-W. Lee, *ACS Appl. Mater. Interfaces*, 2015, **7**, 3117–3125.

128 T.-H. Han, Y.-H. Kim, M. H. Kim, W. Song and T.-W. Lee, *ACS Appl. Mater. Interfaces*, 2016, **8**, 6152–6163.

129 L. Qiu, J. Deng, X. Lu, Z. Yang and H. Peng, *Angew. Chem., Int. Ed.*, 2014, **53**, 10425–10428.

130 S. He, L. Qiu, X. Fang, G. Guan, P. Chen, Z. Zhang and H. Peng, *J. Mater. Chem. A*, 2015, **3**, 9406–9410.

131 H. Jang, Y. J. Park, X. Chen, T. Das, M.-S. Kim and J.-H. Ahn, *Adv. Mater.*, 2016, **28**, 4184–4202.

132 X. Wang, Z. Li, W. Xu, S. A. Kulkarni, S. K. Batabyal, S. Zhang, A. Cao and L. H. Wong, *Nano Energy*, 2015, **11**, 728–735.

133 M. Lee, Y. Jo, D. S. Kim and Y. Jun, *J. Mater. Chem. A*, 2015, **3**, 4129–4133.

134 J. Troughton, D. Bryant, K. Wojciechowski, M. J. Carnie, H. Snaith, D. A. Worsley and T. M. Watson, *J. Mater. Chem. A*, 2015, **3**, 9141–9145.

135 Y. Xiao, G. Han, H. Zhou and J. Wu, *RSC Adv.*, 2016, **6**, 2778–2784.

136 M. Lee, Y. Jo, D. S. Kim, H. Y. Jeong and Y. Jun, *J. Mater. Chem. A*, 2015, **3**, 14592–14597.

137 J. Deng, L. Qiu, X. Lu, Z. Yang, G. Guan, Z. Zhang and H. Peng, *J. Mater. Chem. A*, 2015, **3**, 21070–21076.

138 M. Lee, Y. Ko and Y. Jun, *J. Mater. Chem. A*, 2015, **3**, 19310–19313.

139 F. Zhao, D. Chen, S. Chang, H. Huang, K. Tong, C. Xiao, S. Chou, H. Zhong and Q. Pei, *J. Mater. Chem. C*, 2017, **5**, 531–538.

140 S. Y. Lee, Y. S. Nam, J. C. Yu, S. Lee, E. D. Jung, S. H. Kim, S. Lee, J. Y. Kim and M. H. Song, *ACS Appl. Mater. Interfaces*, 2019, **11**, 39274–39282.

141 M. Lu, H. Wu, X. Zhang, H. Wang, Y. Hu, V. L. Colvin, Y. Zhang and W. W. Yu, *ChemNanoMat*, 2019, **5**, 313–317.

142 Y.-S. Liu, S. Guo, F.-S. Yi, J. Feng and H.-B. Sun, *Opt. Lett.*, 2018, **43**, 5524–5527.

143 H. Lu, J. Sun, H. Zhang, S. Lu and W. C. H. Choy, *Nanoscale*, 2016, **8**, 5946–5953.

144 L. Qiu, L. K. Ono and Y. Qi, *Mater. Today Energy*, 2018, **7**, 169–189.

145 T.-H. Han, J.-W. Lee, C. Choi, S. Tan, C. Lee, Y. Zhao, Z. Dai, N. De Marco, S.-J. Lee, S.-H. Bae, Y. Yuan, H. M. Lee, Y. Huang and Y. Yang, *Nat. Commun.*, 2019, **10**, 520.